RCN核理1a 勉強会
2013.1.10 by A. Tamii

Measurement of the Neutron Radius of ^{208}Pb through Parity Violation in Electron Scattering (PREX)

S. Abrahamyan et al.,
Phys. Rev. Lett. 108, 112502 (2012)

http://prl.aps.org/abstract/PRL/v108/i11/e112502

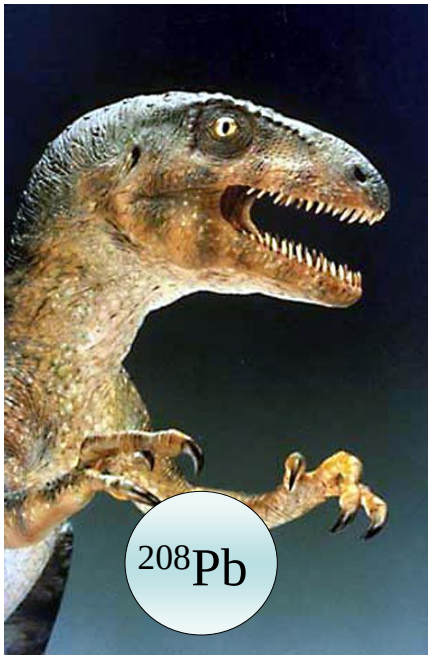

Lead (^{208}Pb) Radius Experiment: PREX

PRL 108, 112502 (2012) PHYSICAL REVIEW LETTERS week ending 16 MARCH 2012

Measurement of the Neutron Radius of ^{208}Pb through Parity Violation in Electron Scattering

S. Abrahamyan,[38] Z. Ahmed,[29] H. Albataineh,[17] K. Aniol,[2] D. S. Armstrong,[5] W. Armstrong,[31] T. Averett,[5] B. Babineau,[19] A. Barbieri,[36] V. Bellini,[11] R. Beminiwattha,[23] J. Benesch,[32] F. Benmokhtar,[6] T. Bielarski,[34] W. Boeglin,[7] A. Camsonne,[32] M. Canan,[24] P. Carter,[6] G. D. Cates,[36] C. Chen,[8] J.-P. Chen,[32] O. Hen,[30] F. Cusanno,[13,†] M. M. Dalton,[36] R. De Leo,[10] K. de Jager,[32,36] W. Deconinck,[21,5] P. Decowski,[28] X. Deng,[36] A. Deur,[32] D. Dutta,[22] A. Etile,[17] D. Flay,[31] G. B. Franklin,[3] M. Friend,[3] S. Frullani,[13] E. Fuchey,[4,31] F. Garibaldi,[13] E. Gasser,[17] R. Gilman,[26] A. Giusa,[11] A. Glamazdin,[16] J. Gomez,[32] J. Grames,[32] C. Gu,[36] O. Hansen,[32] J. Hansknecht,[32] D. W. Higinbotham,[32] R. S. Holmes,[29] T. Holmstrom,[19] C. J. Horowitz,[14] J. Hoskins,[5] J. Huang,[21] C. E. Hyde,[24,4] F. Itard,[17] C.-M. Jen,[29] E. Jensen,[5] G. Jin,[36] S. Johnston,[33] A. Kelleher,[21] K. Kliakhandler,[30] P. M. King,[23] S. Kowalski,[21] K. S. Kumar,[33] J. Leacock,[37] J. Leckey IV,[5] J. H. Lee,[5,23] J. J. LeRose,[32] R. Lindgren,[36] N. Liyanage,[36] N. Lubinsky,[25] J. Mammei,[33] F. Mammoliti,[13] D. J. Margaziotis,[2] P. Markowitz,[7] A. McCreary,[32] D. McNulty,[33] L. Mercado,[33] Z.-E. Meziani,[31] R. W. Michaels,[32] M. Mihovilovic,[15] N. Muangma,[21] C. Muñoz-Camacho,[4] S. Nanda,[32] V. Nelyubin,[36] N. Nuruzzaman,[22] Y. Oh,[27] A. Palmer,[19] D. Parno,[3] K. D. Paschke,[36] S. K. Phillips,[34] B. Poelker,[32] R. Pomatsalyuk,[16] M. Posik,[31] A. J. R. Puckett,[20] B. Quinn,[3] A. Rakhman,[29] P. E. Reimer,[1] S. Riordan,[36] P. Rogan,[33] G. Ron,[18] G. Russo,[11] K. Saenboonruang,[36] A. Saha,[32,*] B. Sawatzky,[32] A. Shahinyan,[38,32] R. Silwal,[36] S. Sirca,[15] K. Slifer,[34] P. Solvignon,[32] P. A. Souder,[29,‡] M. L. Sperduto,[11] R. Subedi,[36] R. Suleiman,[32] V. Sulkosky,[21] C. M. Sutera,[11] W. A. Tobias,[36] W. Troth,[19] G. M. Urciuoli,[12] B. Waidyawansa,[23] D. Wang,[36] J. Wexler,[33] R. Wilson,[9] B. Wojtsekhowski,[32] X. Yan,[35] H. Yao,[31] Y. Ye,[35] Z. Ye,[8,36] V. Yim,[33] L. Zana,[29] X. Zhan,[1] J. Zhang,[32] Y. Zhang,[26] X. Zheng,[36] and P. Zhu[35]

(PREX Collaboration)

Abstract

We report the first measurement of the parity-violating asymmetry A_{PV} in the elastic scattering of polarized electrons from ^{208}Pb. A_{PV} is sensitive to the radius of the neutron distribution (R_n). The result $A_{PV} = 0.656 \pm 0.060(\text{stat}) \pm 0.014(\text{syst})$ ppm corresponds to a difference between the radii of the neutron and proton distributions $R_n - R_p = 0.33^{+0.16}_{-0.18}$ fm and provides the first electroweak observation of the neutron skin which is expected in a heavy, neutron-rich nucleus.

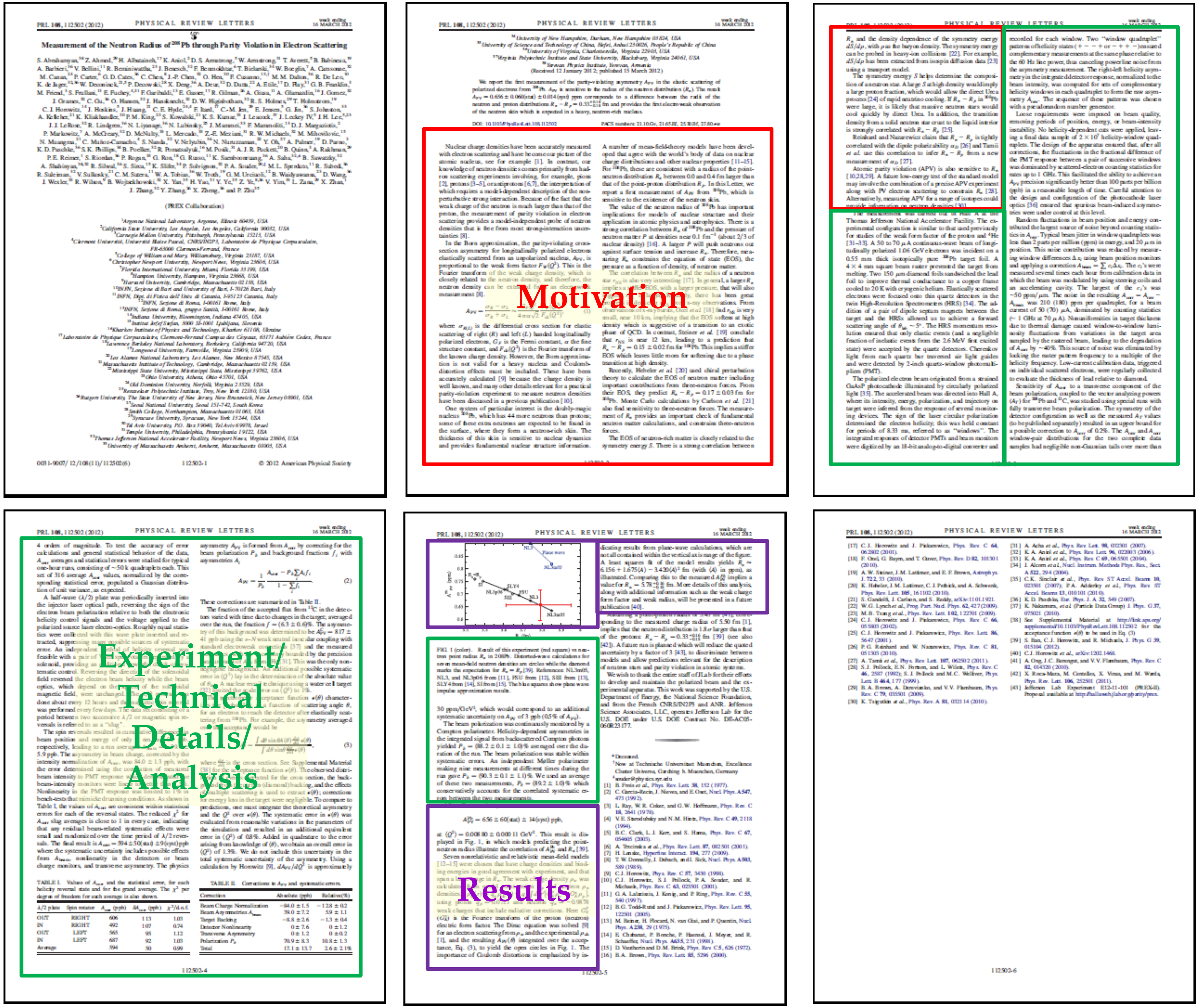
Motivation
Experiment/
Technical
Details/
Analysis
Results

Motivation

Proton/Neutron Density Distribution, Neutron Skin

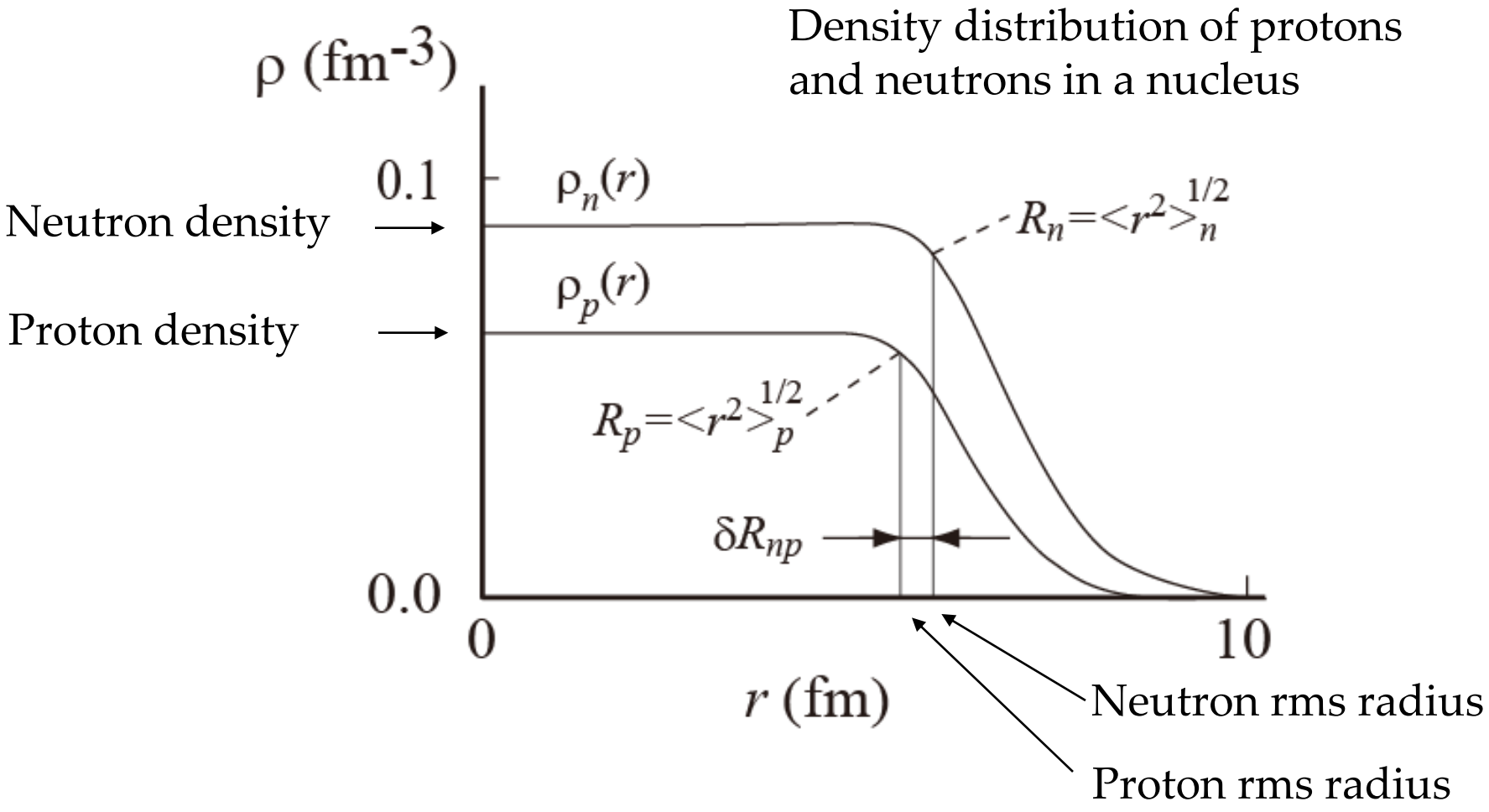

Nuclear charge density (distribution)

Studied by electron (elastic) scattering [1]

Neutron density (distribution)

Studied by hadron scattering

pion scattering [2]
proton scattering [3-5]
anti-proton absorption (X-ray observation) [6,7]

requires <u>model-dependent description of strong interaction.</u>

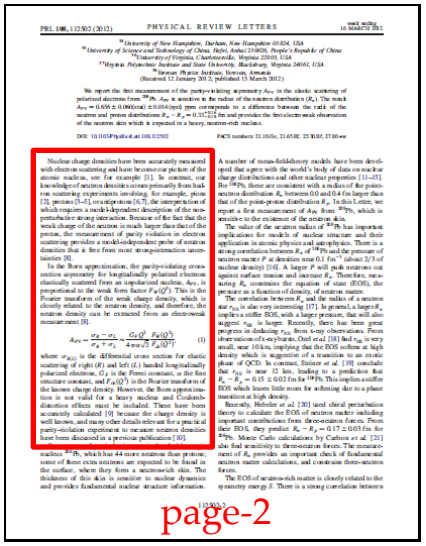
PHYSICAL REVIEW LETTERS

Nuclear charge densities have been accurately measured with electron scattering and have become our picture of the atomic nucleus, see for example [1]. In contrast, our knowledge of neutron densities comes primarily from hadron scattering experiments involving, for example, pions [2], protons [3–5], or antiprotons [6,7], the interpretation of which requires a model-dependent description of the nonperturbative strong interaction. Because of the fact that the weak charge of the neutron is much larger than that of the proton, the measurement of parity violation in electron scattering provides a model-independent probe of neutron densities that is free from most strong-interaction uncertainties [8].

In the Born approximation, the parity-violating cross-section asymmetry for longitudinally polarized electrons elastically scattered from an unpolarized nucleus, A_{PV}, is proportional to the weak form factor $F_W(Q^2)$. This is the Fourier transform of the weak charge density, which is closely related to the neutron density, and therefore, the neutron density can be extracted from an electroweak measurement [8].

$$A_{PV} = \frac{\sigma_R - \sigma_L}{\sigma_R + \sigma_L} \approx \frac{G_F Q^2}{4\pi\alpha\sqrt{2}} \frac{F_W(Q^2)}{F_E(Q^2)} \quad (1)$$

where $\sigma_{R(L)}$ is the differential cross section for elastic scattering of right (R) and left (L) handed longitudinally polarized electrons, G_F is the Fermi constant, α the fine structure constant, and $F_E(Q^2)$ is the Fourier transform of the known charge density. However, the Born approximation is not valid for a heavy nucleus and Coulomb-distortion effects must be included. These have been accurately calculated [9] because the charge density is well known, and many other details relevant for a practical parity-violation experiment to measure neutron densities have been discussed in a previous publication [10].

nucleus ^{208}Pb, which has 44 more neutrons than protons; some of these extra neutrons are expected to be found in the surface, where they form a neutron-rich skin. The thickness of this skin is sensitive to nuclear dynamics and provides fundamental nuclear structure information.

A number of mean-field-theory models have been developed that agree with the world's body of data on nuclear charge distributions and other nuclear properties [11–15]. For ^{208}Pb, these are consistent with a radius of the point-neutron distribution R_n between 0.0 and 0.4 fm larger than that of the point-proton distribution R_p. In this Letter, we report a first measurement of A_{PV} from ^{208}Pb, which is sensitive to the existence of a neutron skin.

The value of the neutron radius of ^{208}Pb has important implications for models of nuclear structure and their application in atomic physics and astrophysics. There is a strong correlation between R_n of ^{208}Pb and the pressure of neutron matter P at densities near 0.1 fm^{-3} (about 2/3 of nuclear density) [16]. A larger P will push neutrons out against surface tension and increase R_n. Therefore, measuring R_n constrains the equation of state (EOS), the pressure as a function of density, of neutron matter.

The correlation between R_n and the radius of a neutron star r_{NS} is also very interesting [17]. In general, a larger R_n implies a stiffer EOS, with a larger pressure, that will also suggest r_{NS} is larger. Recently, there has been great progress in deducing r_{NS} from x-ray observations. From observations of x-ray bursts, Özel *et al.* [18] find r_{NS} is very small, near 10 km, implying that the EOS softens at high density which is suggestive of a transition to an exotic phase of QCD. In contrast, Steiner *et al.* [19] conclude that r_{NS} is near 12 km, leading to a prediction that $R_n - R_p \approx 0.15 \pm 0.02$ fm for ^{208}Pb. This implies a stiffer EOS which leaves little room for softening due to a phase transition at high density.

Recently, Hebeler *et al.* [20] used chiral perturbation theory to calculate the EOS of neutron matter including important contributions from three-neutron forces. From their EOS, they predict $R_n - R_p = 0.17 \pm 0.03$ fm for ^{208}Pb. Monte Carlo calculations by Carlson *et al.* [21] also find sensitivity to three-neutron forces. The measurement of R_n provides an important check of fundamental neutron matter calculations, and constrains three-neutron forces.

The EOS of neutron-rich matter is closely related to the symmetry energy S. There is a strong correlation between

page-2

Charge Density (Electron Scattering)

[1] B. Frois et al, PRL38, 152(1977)

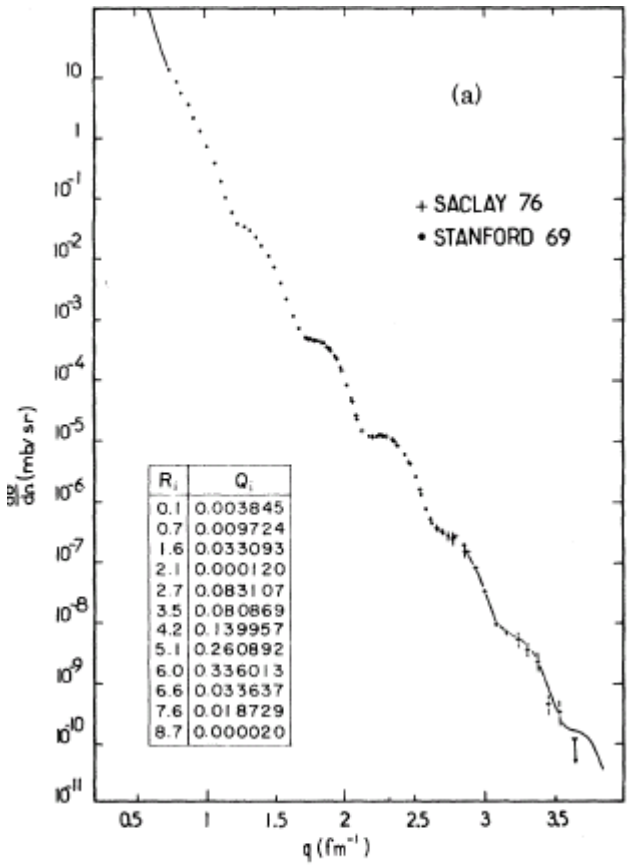

R_i	Q_i
0.1	0.003845
0.7	0.009724
1.6	0.033093
2.1	0.000120
2.7	0.083107
3.5	0.080869
4.2	0.139957
5.1	0.260892
6.0	0.336013
6.6	0.033637
7.6	0.018729
8.7	0.000020

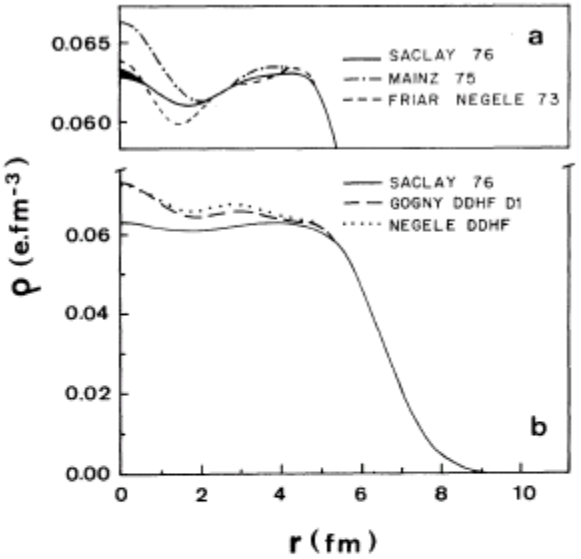

FIG. 2. (a) Charge density determined by present analysis and Refs. 7 and 8. The systematical uncertainties of the data allow an overall shift of ±0.8% for ($r < 4$ fm) without sizeable influence on the details of the structure. (b) Present density compared to density-dependent HF densities of Refs. 13 and 22. The scale of (a) is expanded by a factor of 4.

charge radius: 5.50 fm
point proton radius: 5.45 fm
(by using formula in [41])

Neutron Density (Proton Scattering)

Not Referred

[4] V.E. Starodubsky et al., PRC18, 2641(1994)

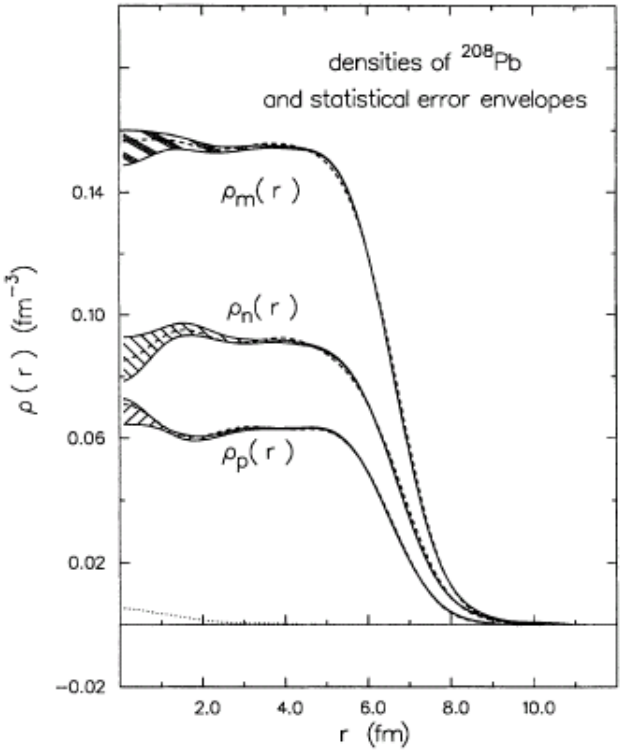

FIG. 6. Extracted neutron and matter densities for ^{208}Pb lying in the middle of the corresponding statistical error bands (the hatched areas). The HF proton, neutron, and matter densities are depicted by the dashed lines. The proton density obtained by unfolding the charge density of Ref. [43] is also shown with its statistical error envelope. The dotted line at the bottom is for the statistical error band obtained with the SOG method of Ref. [23].

R_{ch}=5.503(2), R_p=5.458, R_n=5.655(42) fm

R_n-R_p=0.197(42) fm

J. Zenihiro et al., PRC82, 044611 (2010)

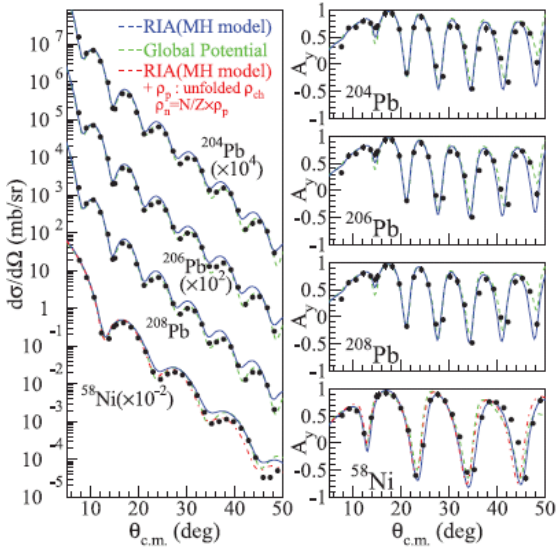

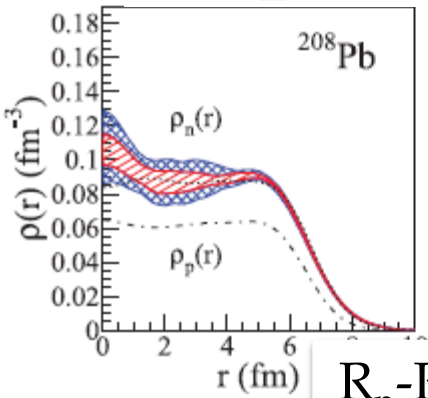

standard error-envelope

error-envelope w/ model uncertainty

$\rho_n(r)$: DH

$\rho_p(r)$: unfolded ρ_{ch}

R_n-R_p=0.211 $^{+0.026}_{-0.029}$ $^{+0.054}_{-0.063}$ fm

Nucleus	r_{ch}	r_p^{unfold}	r_n	δr_n^{std}	δr_n^{mdl}
^{204}Pb	5.479(2)	5.420(2)	5.598	$^{+0.029}_{-0.020}$	$^{+0.047}_{-0.059}$
^{206}Pb	5.490(2)	5.433(2)	5.613	$^{+0.026}_{-0.026}$	$^{+0.048}_{-0.064}$
^{208}Pb	5.503(2)	5.442(2)	5.653	$^{+0.026}_{-0.029}$	$^{+0.054}_{-0.063}$

Neutron Density (anti-protonic atom X-ray)

Not Referred

[6] A. Trzcinska et al., PRL87, 082501(2001)

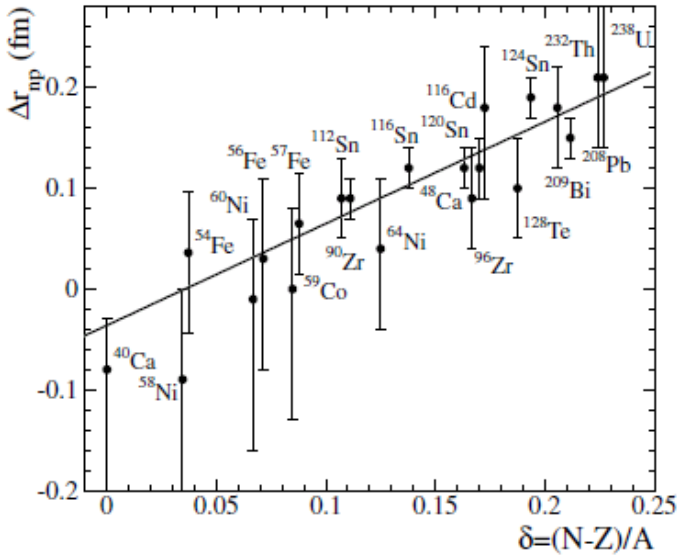

FIG. 4. Difference Δr_{np} between the rms radii of the neutron and proton distributions as deduced from the antiprotonic atom x-ray data, as a function of $\delta = (N - Z)/A$. The proton distributions were obtained from electron scattering data [41] (Sn nuclei) or from muonic atom data [38,42,43] (other nuclei). The full line represents the linear relationship between δ and Δr_{np} as obtained from a fit to the experimental data.

B. Kłos *et al.*, PRC76, 014311(2009)

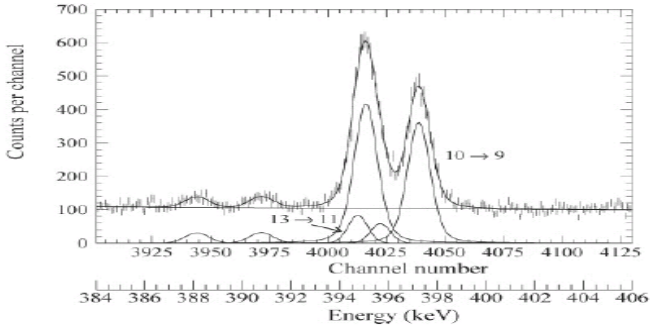

FIG. 3. Part of the antiprotonic x-ray spectrum measured for ^{208}Pb using the detector with the 1035 mm^2 × 14 mm crystal. The fit to the broadened 10 → 9 transition is also shown. The 13 → 11 line is admixed to the 10 → 9 line.

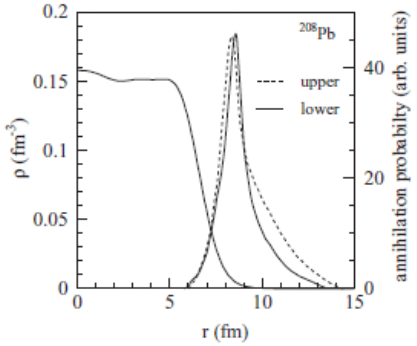

FIG. 10. $\bar{p}$ annihilation probability (arbitrary units) from the upper and lower states for the antiprotonic ^{208}Pb atom. The matter density (DD-ME2) in ^{208}Pb is also shown. The calculations of the annihilation probability were done with the Batty zero-range potential and 2pF parametrization of the DD-ME2 density (cf. Table VI).

Widths and shifts of the levels due to the strong interaction
→ antiproton-nucleus optical potential
assumes two-parameter Fermi distribution

$$R_n\text{-}R_p = 0.16 \pm (0.02)_{stat} \pm (0.04)_{syst}$$

Nuclear charge density (distribution)

Studied by electron (elastic) scattering [1]

Neutron density (distribution)

Studied by hadron scattering

pion scattering [2]
proton scattering [3-5]
anti-proton absorption (X-ray observation) [6,7]

requires <u>model-dependent description of strong interaction.</u>

Parity violating (PV) electron scattering by weak interaction:
"model-independent probe"

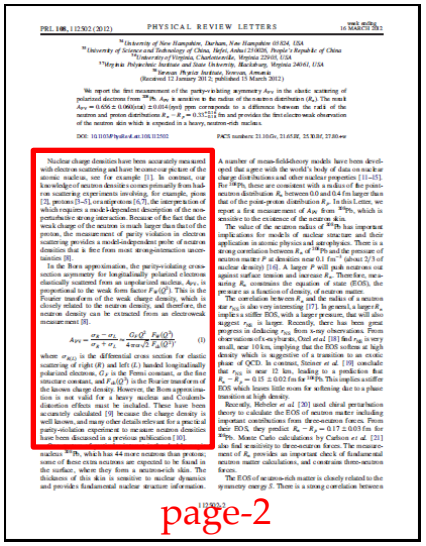
page-2

Parity Violating (PV) Cross Section Asymmetry in Electron Scattering [8]

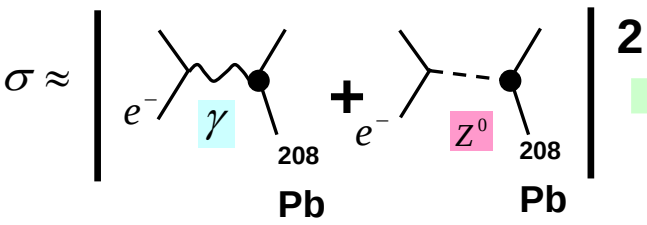

A_{PV} from interference

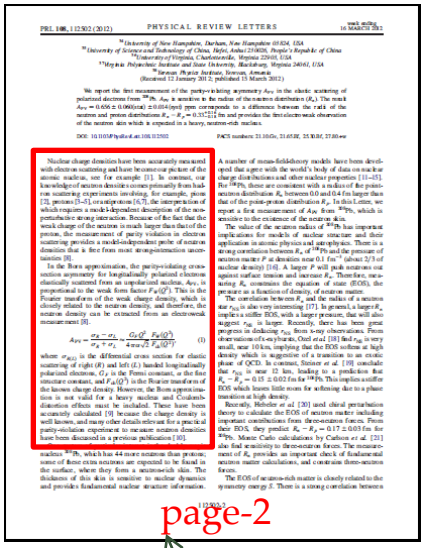
page-2

$$A_{PV} = \frac{\sigma_R - \sigma_L}{\sigma_R + \sigma_L} \approx \frac{G_F Q^2}{4\pi\alpha\sqrt{2}} \frac{F_W(Q^2)}{F_{ch}(Q^2)}, \qquad (1)$$

in PWBA

R (L): Right (Left) helicity

longitudinal polarization

interference between EM and weak interactions

G_F: Fermi coupling constant
α: fine structure constant
Q: four-momentum transfer $(\omega,\mathbf{q})$
F_W: weak form factor
F_{ch}: charge form factor

Fourier transform of the weak charge density

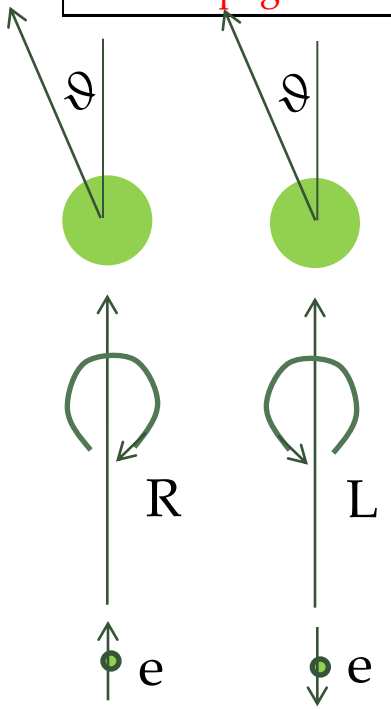

helicity

Coulomb distortion effect is included in the real analysis [9], also other effects [10].

Weak Charge

J-F. Rajotte, arxiv:1110.2218v1

TABLE I: Electroweak Couplings of u and d Quarks and Nucleons as Function of the Weak Mixing Angle θ_W

Particles	EM Charge	Weak Charge
u	$+\frac{2}{3}$	$1-\frac{8}{3}\sin^2\theta_W$
d	$-\frac{1}{3}$	$-1+\frac{4}{3}\sin^2\theta_W$
$p(uud)$	$+1$	$1-4\sin^2\theta_W$
$n(udd)$	0	-1

in the standard model

~ 0.08 0.0721

-0.9878

↑

with radiative correction

ϑ_w: Weinberg Angle or Weak Mixing Angle

$\sin^2\vartheta_w$=0.23116(12) c.f. PDG 2012

$$\begin{pmatrix}\gamma\\ Z^0\end{pmatrix}=\begin{pmatrix}\cos\theta_W & \sin\theta_W\\ -\sin\theta_W & \cos\theta_W\end{pmatrix}\begin{pmatrix}B^0\\ W^0\end{pmatrix}$$

Weak charge distribution is primarily determined by the neutron distribution

BUT weak interaction is VERY weak...

APV ~ 656 ppb = 0.000000656

Backup Slides

Standard Model

TABLE 13.1
Weak Isospin and Hypercharge Quantum Numbers of Leptons and Quarks

Lepton	T	T^3	Q	Y
ν_e	$\frac{1}{2}$	$\frac{1}{2}$	0	-1
e_L^-	$\frac{1}{2}$	$-\frac{1}{2}$	-1	-1
e_R^-	0	0	-1	-2

Quark	T	T^3	Q	Y
u_L	$\frac{1}{2}$	$\frac{1}{2}$	$\frac{2}{3}$	$\frac{1}{3}$
d_L	$\frac{1}{2}$	$-\frac{1}{2}$	$-\frac{1}{3}$	$\frac{1}{3}$
u_R	0	0	$\frac{2}{3}$	$\frac{4}{3}$
d_R	0	0	$-\frac{1}{3}$	$-\frac{2}{3}$

$$Q = T^3 + \frac{Y}{2}$$

$$j_\mu^{em} = J_\mu^3 + \tfrac{1}{2} j_\mu^Y .$$

Backup Slides

Electro-weak Interaction

$$-i\,g(J^i)^\mu W_\mu^i - i\,\frac{g'}{2}(j^Y)^\mu B_\mu.$$

charged fields

$$W_\mu^\pm = \sqrt{\tfrac{1}{2}}\left(W_\mu^1 \mp i W_\mu^2\right)$$

neutral fields (mass eigenstates)

$$A_\mu = B_\mu \cos\theta_W + W_\mu^3 \sin\theta_W \qquad \text{(massless)},$$

$$Z_\mu = -B_\mu \sin\theta_W + W_\mu^3 \cos\theta_W \qquad \text{(massive)},$$

⟹ Electro-Magnetic Field

Electro-weak neutral current interaction

$$-igJ_\mu^3(W^3)^\mu - i\frac{g'}{2}j_\mu^Y B^\mu$$

$$= -i\left(g\sin\theta_W J_\mu^3 + g'\cos\theta_W \frac{j_\mu^Y}{2}\right)A^\mu \quad \Longrightarrow \quad -i\,ej_\mu^{em}A^\mu$$

$$-i\left(g\cos\theta_W J_\mu^3 - g'\sin\theta_W \frac{j_\mu^Y}{2}\right)Z^\mu. \quad \Longrightarrow \quad -i\frac{g}{\cos\theta_W}J_\mu^{NC}Z^\mu$$

$$g\sin\theta_W = g'\cos\theta_W = e$$

$$J_\mu^{NC} \equiv J_\mu^3 - \sin^2\theta_W j_\mu^{em}$$

Backup Slides

Electro-magnetic interaction

$$-i\,e\,(j^{em})^{\mu}\,A_{\mu} = -i\,e\,(\bar{\psi}\gamma^{\mu}Q\psi)\,A_{\mu}$$

Vector coupling

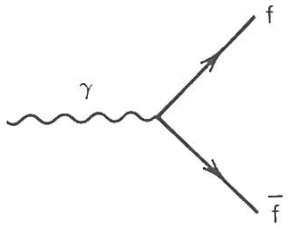

$$-ieQ_f\gamma^{\mu}$$

Electro-weak neutral current interaction

Vector coupling

$$-i\frac{g}{\cos\theta_W}\left(J_{\mu}^{3} - \sin^2\theta_W j_{\mu}^{em}\right)Z^{\mu} =$$

$$-i\frac{g}{\cos\theta_W}\bar{\psi}_f\gamma^{\mu}\left[\tfrac{1}{2}(1-\gamma^5)T^3 - \sin^2\theta_W Q\right]\psi_f Z_{\mu}$$

V-A coupling

produces parity-violation

=L-helicity projection operator

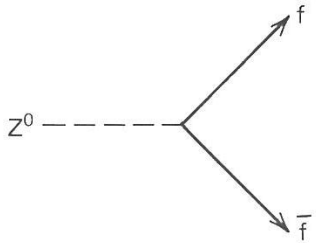

$$-i\frac{g}{\cos\theta_W}\gamma^{\mu}\tfrac{1}{2}\left(c_V^f - c_A^f\gamma^5\right).$$

TAI

The $Z \to f\bar{f}$ Vertex Factors, (13.41), in the Standard Model (with $\sin^2\theta_W = 0.234$)

f	Q_f	c_A^f	c_V^f
$\nu_e, \nu_\mu, \ldots$	0	$\frac{1}{2}$	$\frac{1}{2}$
$e^-, \mu^-, \ldots$	-1	$-\frac{1}{2}$	$-\frac{1}{2} + 2\sin^2\theta_W \simeq -0.03$
u, c, ...	$\frac{2}{3}$	$\frac{1}{2}$	$\frac{1}{2} - \frac{4}{3}\sin^2\theta_W \simeq 0.19$
d, s, ...	$-\frac{1}{3}$	$-\frac{1}{2}$	$-\frac{1}{2} + \frac{2}{3}\sin^2\theta_W \simeq -0.34$

Neutron Skin Thickness of ^{208}Pb

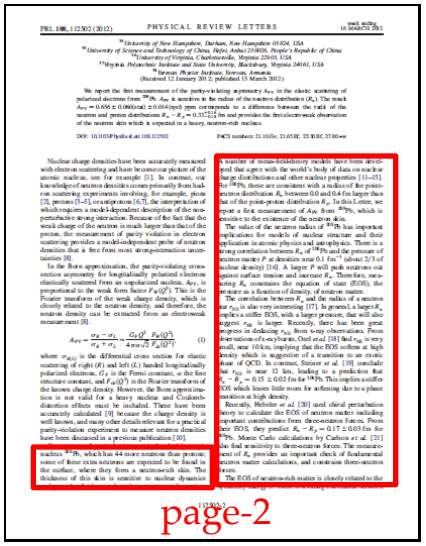
page-2

Doubly magic nucleus

Predicted in the range of 0.0-0.4 fm by various mean-field models. [11-15]

Neutron skin thickness:

sensitive to nuclear dynamics, fundamental nuclear-structure information
atomic physics
astrophysics

strong correlation

R_n-R_p (^{208}Pb) ⟷ Pressure of neutron matter at ρ~0.1 fm^{-3}

neutron matter EOS

⟷ Density dep. of the symmetry energy

$dS/d\rho$ ($\propto$L)

⟷ Neutron star radius (r_{NS})

Neutron Star, Neutron Matter EOS

Neutron Star Mass and Radius (r_{NS})

~10 km x-ray burst observation (Ozel [18])

softer EOS at high ρ ... exotic phase of QCD (strangeness)

~12 km neutron star model and nuclear EOS (Steiner [19])

stiffer EOS (does not support the exotic phase)

R_n-R_p = 0.15 ± 0.02 fm for ^{208}Pb

Observation of a two-solar mass neutron star,
P.B. Demorest et al., Nature 467, 1081(2010)

Not Referred

most of EOS inc. the exotic phase fail to reproduce the existence.

Chiral perturbation theory from few-body calc. inc. 3NF
(Hebeler [20], Carlson [21])

R_n-R_p = 0.17 ± 0.03 fm for ^{208}Pb

[18] F. Ozel et al., PRD82,101301(2010)

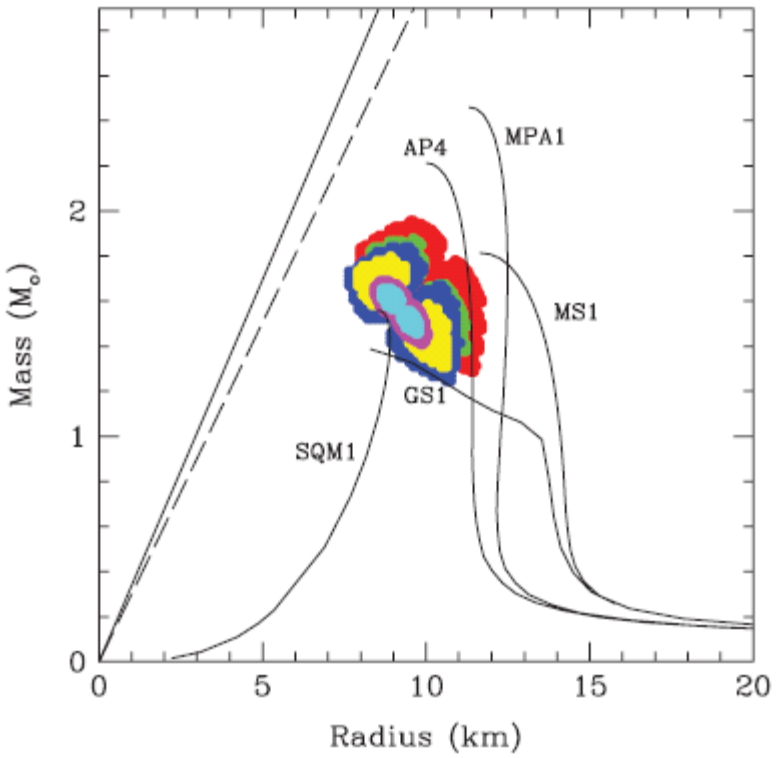

FIG. 1 (color). The 1- and 2-σ confidence contours for the masses and radii of three neutron stars in the binaries 4U 1608 − 248 (green/red), EXO 1745 − 248 (yellow/blue), and 4U 1820 − 30 (cyan/magenta), compared with predictions of representative EoS (see text for details). The details of the measurements are described in Ref. [3]. The diagonal lines are the black-hole event horizon (solid line) and Buchdahl (dashed line) [29] limits.

AP4: AV18+UIX-3NF+rel.boost

MPA1: Dirac Brueckner Hartree Fock

MS1: Relativistic Mean Field

GS1: RMT plus kaons

SQM1: u,d,s quark matter

[19] A.W. Steiner et al., Astro J. 722_33(2010)

A.W. Steiner et al., arXiv:1205.6871v1

"Ozel et al. [6] considered only PRE sources, but these may be subject to considerable systematic errors [7, 9, 10]." PRE: photospheric radius expansion

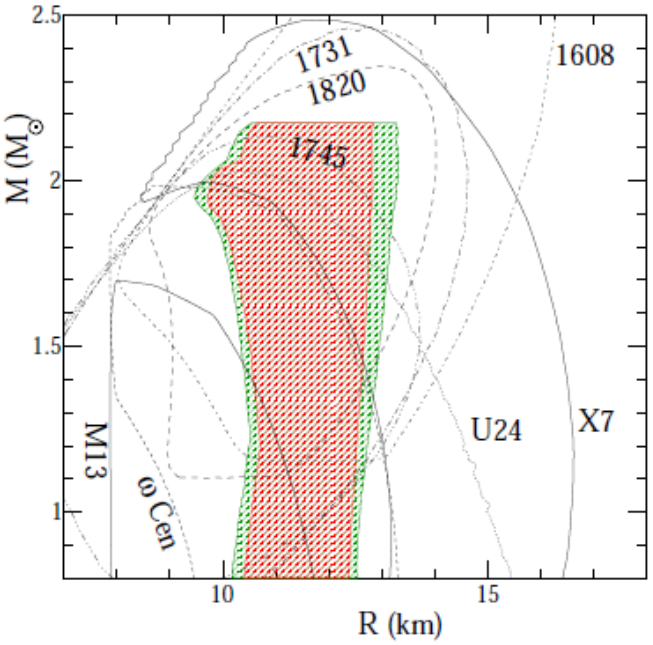

FIG. 1: A comparison of the predicted M–R relation with the observations. The shaded regions outline the 68% and 95% confidences for the M–R relation; these include variations in the EOS model and the modifications to the data set (see Table I) but not the more speculative scenarios. The lines give the 95% confidence regions for the eight neutron stars in our data set.

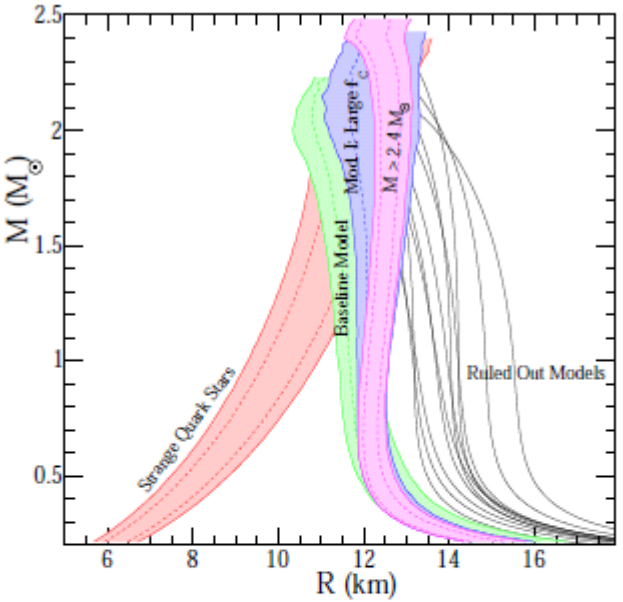

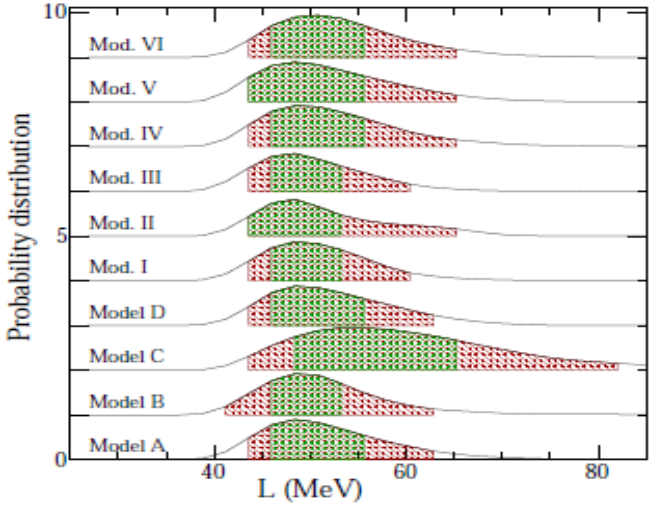

FIG. 4: The limits on the density derivative of the symmetry energy, L. The single-hatched (red) regions show the 95% confidence limits and the double-hatched (green) regions show the 68% confidence limits.

Observation of a Two Solar-Mass Neutron Star Excludes EOS Models with Strangeness

P.B. Demorest et al., Nature 467, 1081(2010)

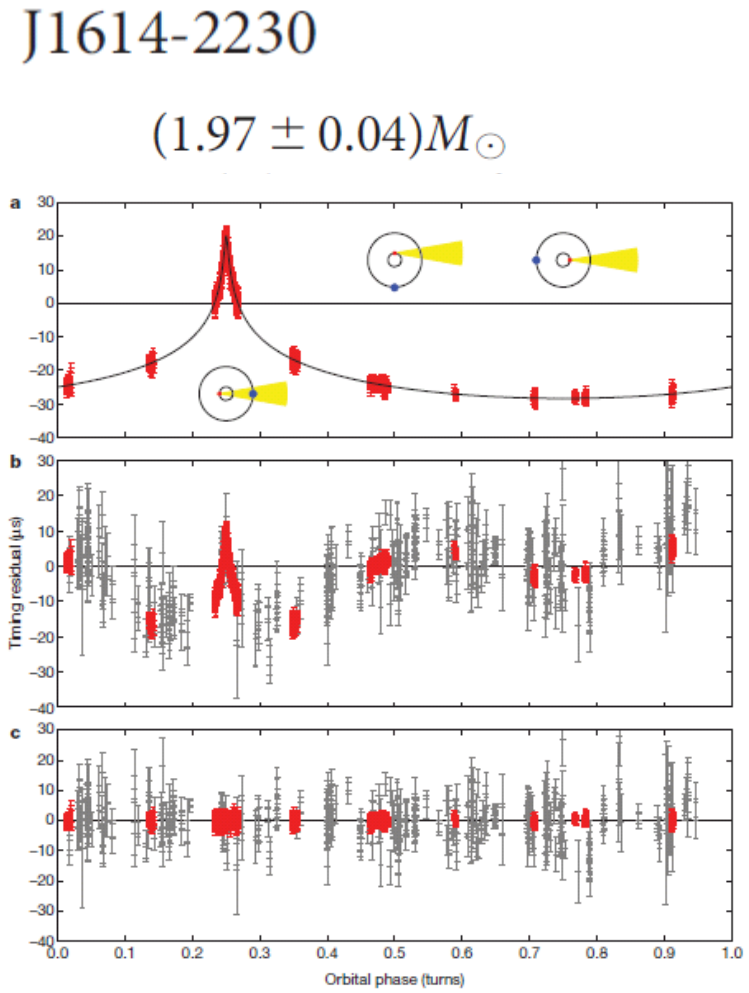

Observation of Shapiro-delay of pulser signals of a neutron star - white dwarf binary.

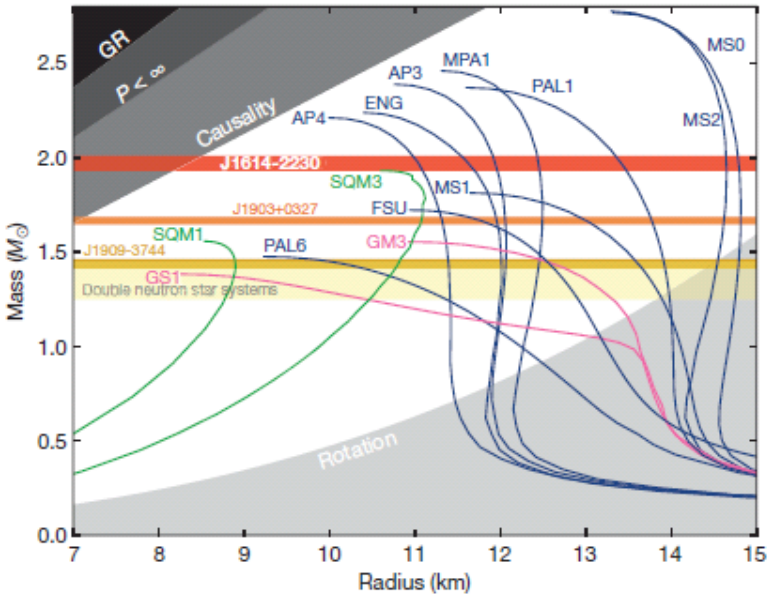

Figure 3 | Neutron star mass–radius diagram. The plot shows non-rotating mass versus physical radius for several typical EOSs[27]: blue, nucleons; pink, nucleons plus exotic matter; green, strange quark matter. The horizontal bands show the observational constraint from our J1614-2230 mass measurement of $(1.97 \pm 0.04)M_\odot$, similar measurements for two other millisecond pulsars[8,28] and the range of observed masses for double neutron star binaries[2]. Any EOS line that does not intersect the J1614-2230 band is ruled out by this measurement. In particular, most EOS curves involving exotic matter, such as kaon condensates or hyperons, tend to predict maximum masses well below $2.0M_\odot$ and are therefore ruled out. Including the effect of neutron star rotation increases the maximum possible mass for each EOS. For a 3.15-ms spin period, this is a $\lesssim 2\%$ correction[29] and does not significantly alter our conclusions. The grey regions show parameter space that is ruled out by other theoretical or observational constraints[2]. GR, general relativity; P, spin period.

Blue: nucleons

Pink: nucleons and exotic matter

Green: strange quark matter

Symmetry Energy, ρ -dependence

Heavy Ion Collision (HIC) [22], isospin diffusion [23]

requires nuclear EOS and symmetry energy.
or constrains the EOS

Neutron star structure:
proton fraction is determined by the symmetry energy
⇔chemical potential difference between a proton and a neutron

solid neutron crust ←→liquid interior transition
⇒ Strongly correlated with R_n-R_p

Neutron star cooling:
large R_n-R_p
⇒rapid cooling of massive n-star by direct Urca process

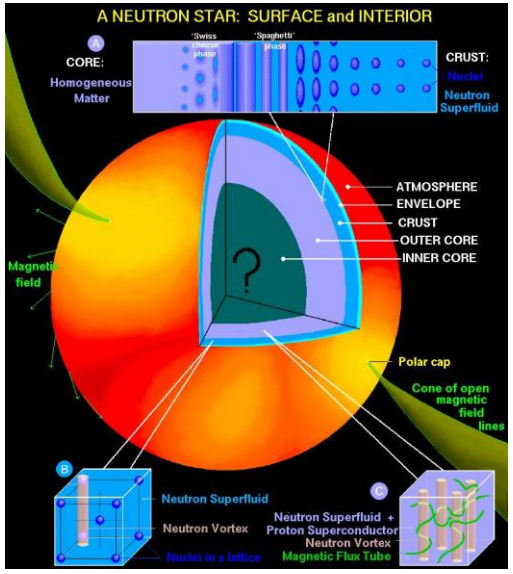

Fig from D. Page. in J.M. Lattimer and M. Prakash, Science 304 (2004) 536.

Neutron Star Cooling by Neutrino Emission

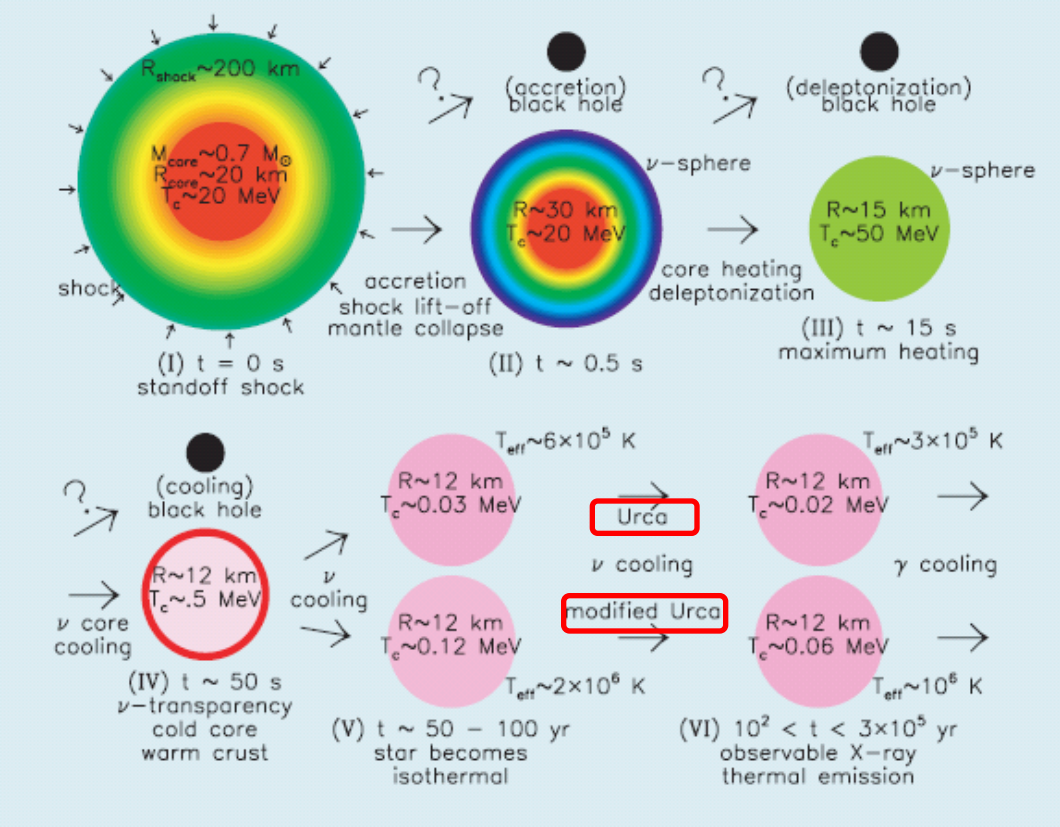

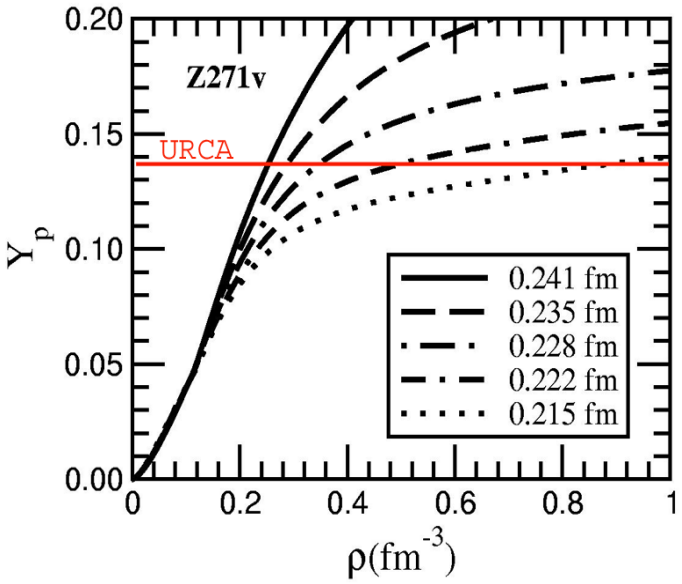

Urca was named after a casino in Rio de Janeiro where gamblers continuously lost money.

Lattimer and Prakash, Science 304, 536 (2004).

Direct Urca Process

$$n \rightarrow p + e^- + \bar{\nu}_e, \quad p \rightarrow n + e^+ + \nu_e$$

takes place only if proton fraction Y_p is large

Modified Urca Process

$$n + (n, p) \rightarrow p + (n, p) + e^- + \bar{\nu}_e.$$
$$p + (n, p) \rightarrow n + (n, p) + e^+ + \nu_e$$

Dipole Polarizability (α_D)

Dipole Polarizability is strongly correlated with R_n-R_p [26]

$$\alpha_D = \frac{\hbar c}{2\pi^2}\int \frac{\sigma_{abs}}{\omega^2}\,d\varpi = \frac{8\pi}{9}\int \frac{dB(E1)}{\omega}$$

R_n-R_p = 0.168 ± 0.022 fm for ^{208}Pb

Determination of α_D by an Electro-Magnetic Probe

including model uncertainty.

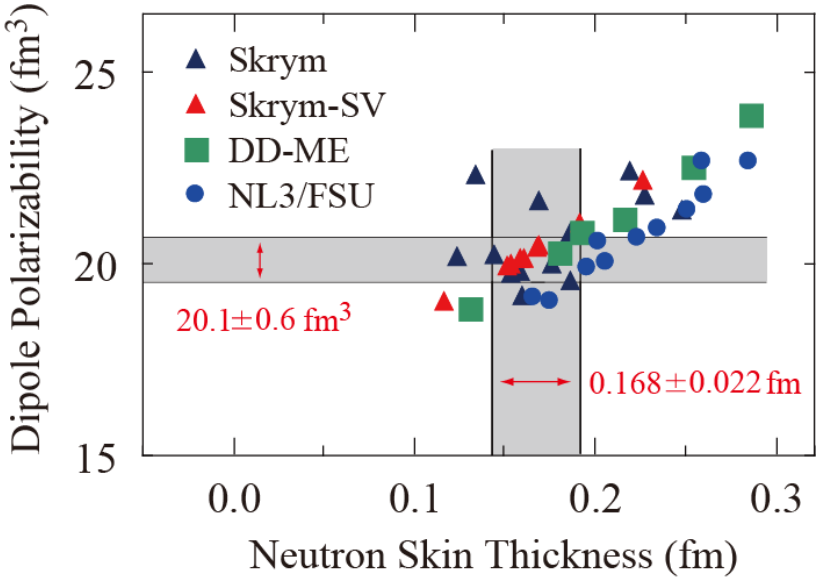

J. Piekarewicz et al., PRC85, 041302(2012)

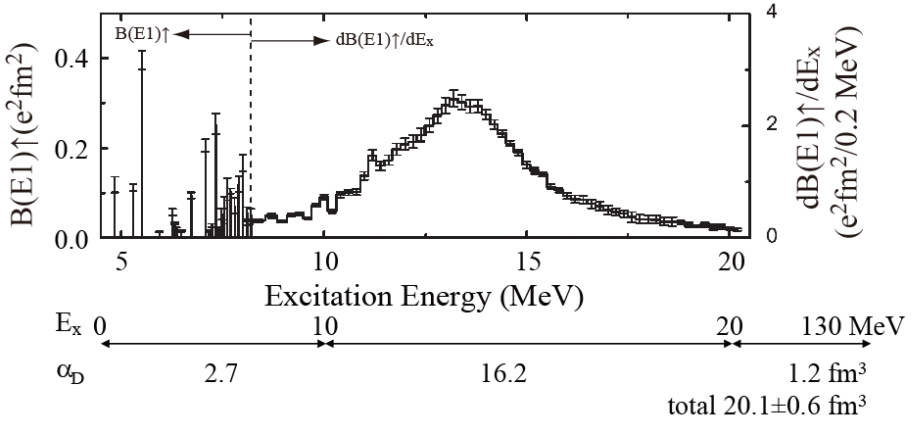

AT et al. PRL107,062502(2011) [27]

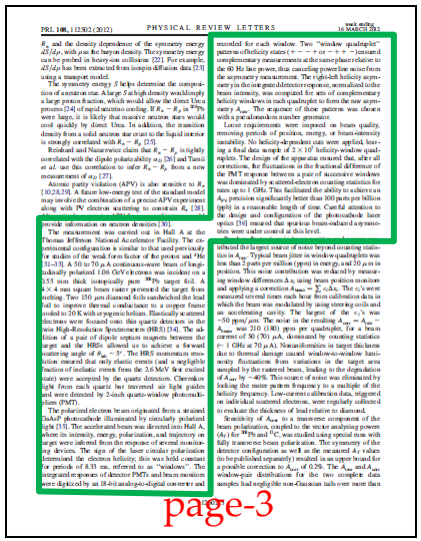

Experiment:

Parity Violating Electron Scattering from ^{208}Pb at J-Lab.

Thomas Jefferson National Accelerator Facility (Jefferson-Lab)

Hall A at Jefferson Lab

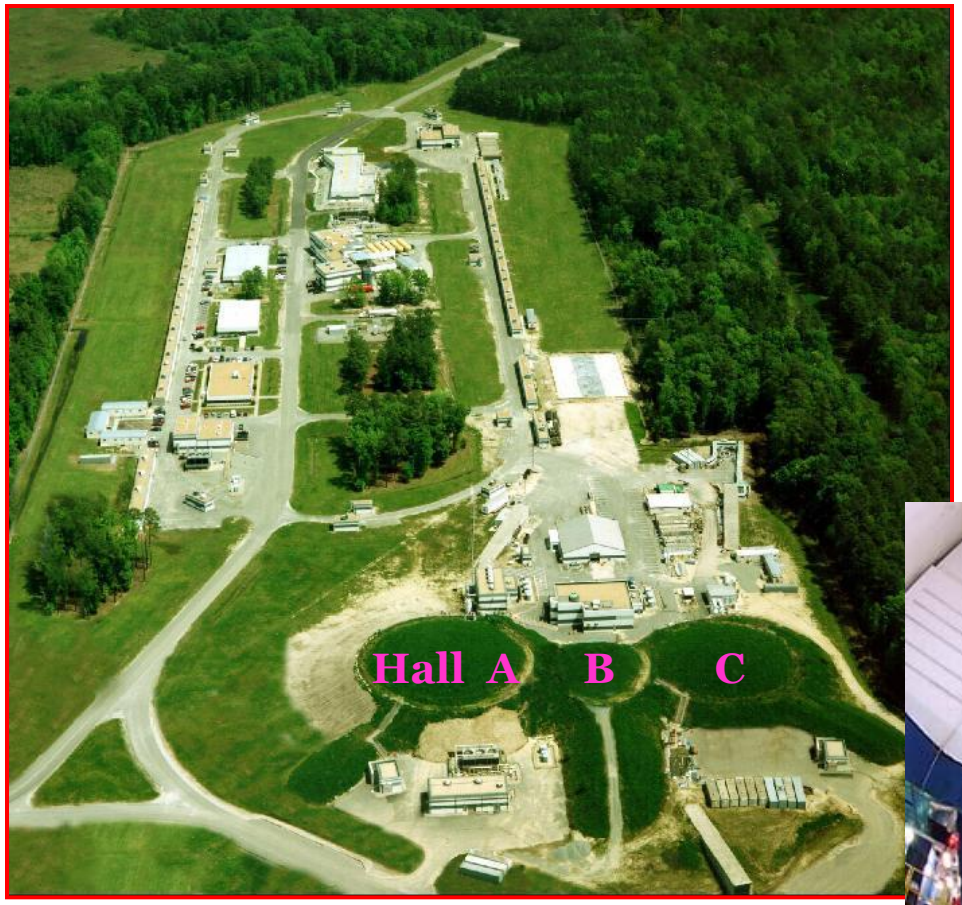

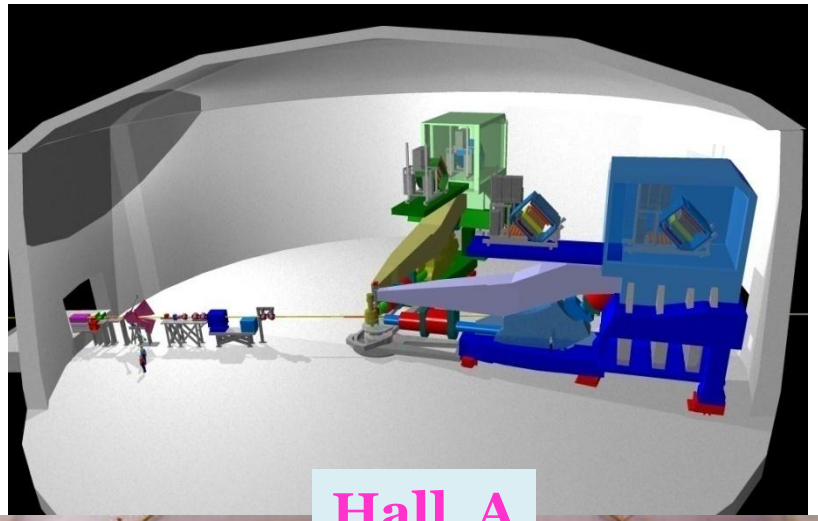

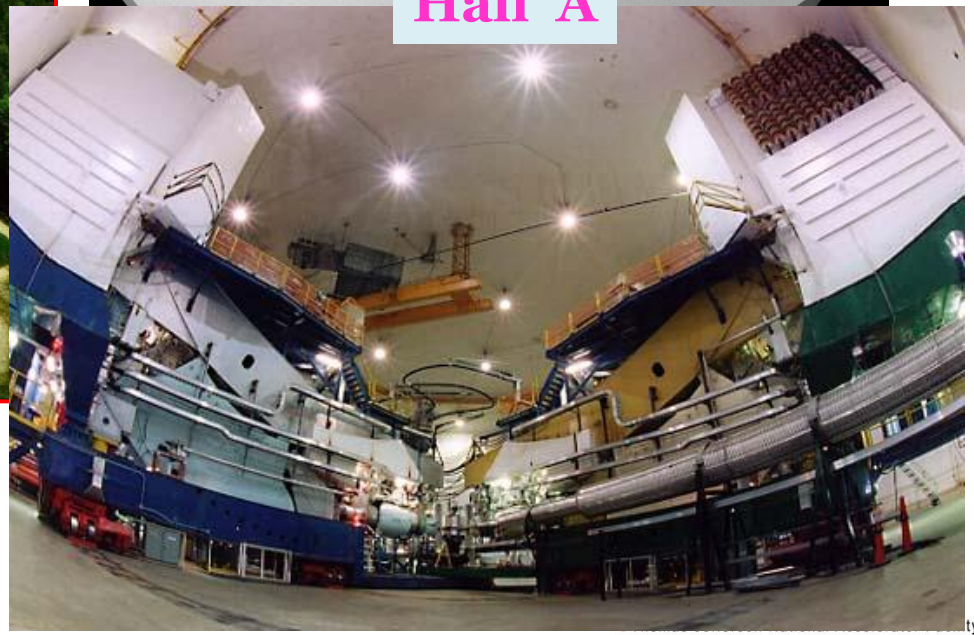

R. Michaels, Jlab
Seminar @ TAMU
Mar 6, 2012

Thomas Jefferson National Accelerator Facility (Jefferson-Lab) Hall-A

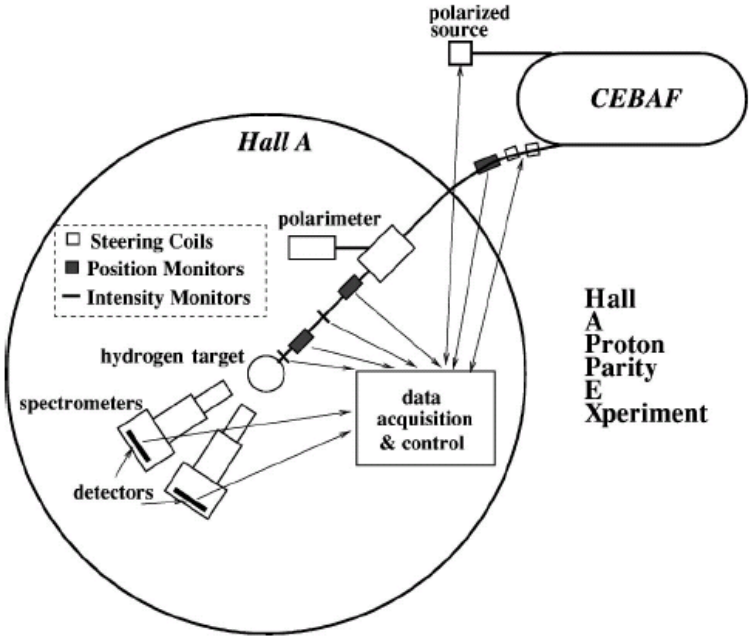

FIG. 1. Schematic overview of the HAPPEX experiment.

K.A. Aniol et al., PRC**69**, 065501 (2004)

HAPPEX: Hall A Precision Parity EXperiment

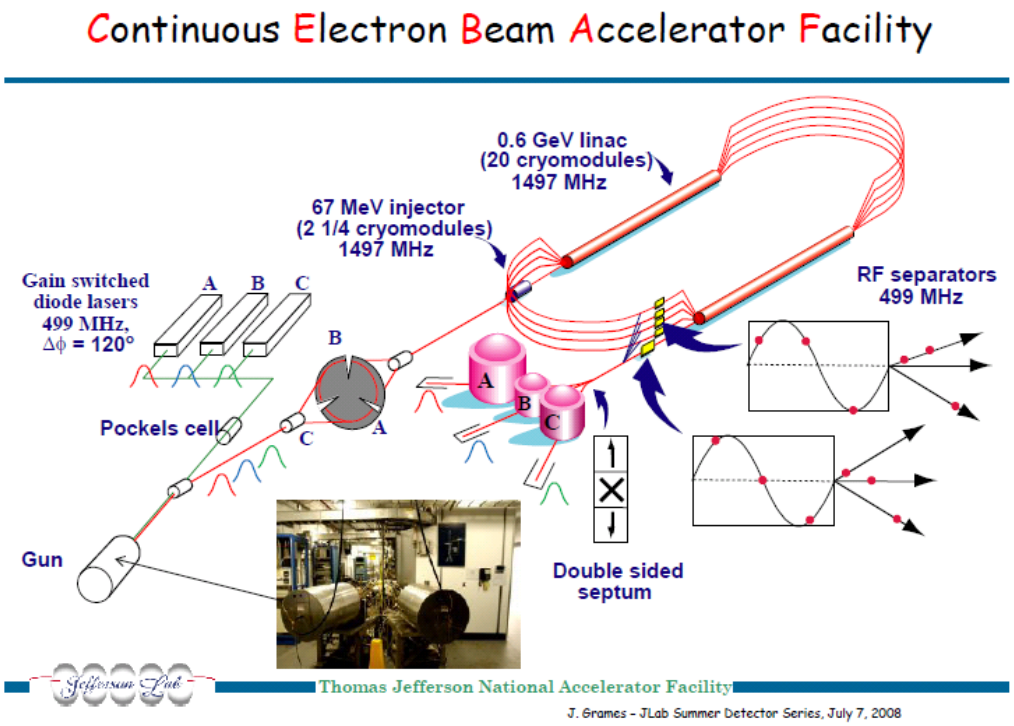

electron beam:

50-70 μA, longitudinal pol., 1.06 GeV
normal spot size 50μm
4×4 mm^2 beam rastering

in PREX, PRL108,112502(2012)

Pol. Electron Sources (Laser System)

linear polarizer and a rotatable λ/2 plate

Gain-switched diode laser (499 MHz), relative phase: 120 deg

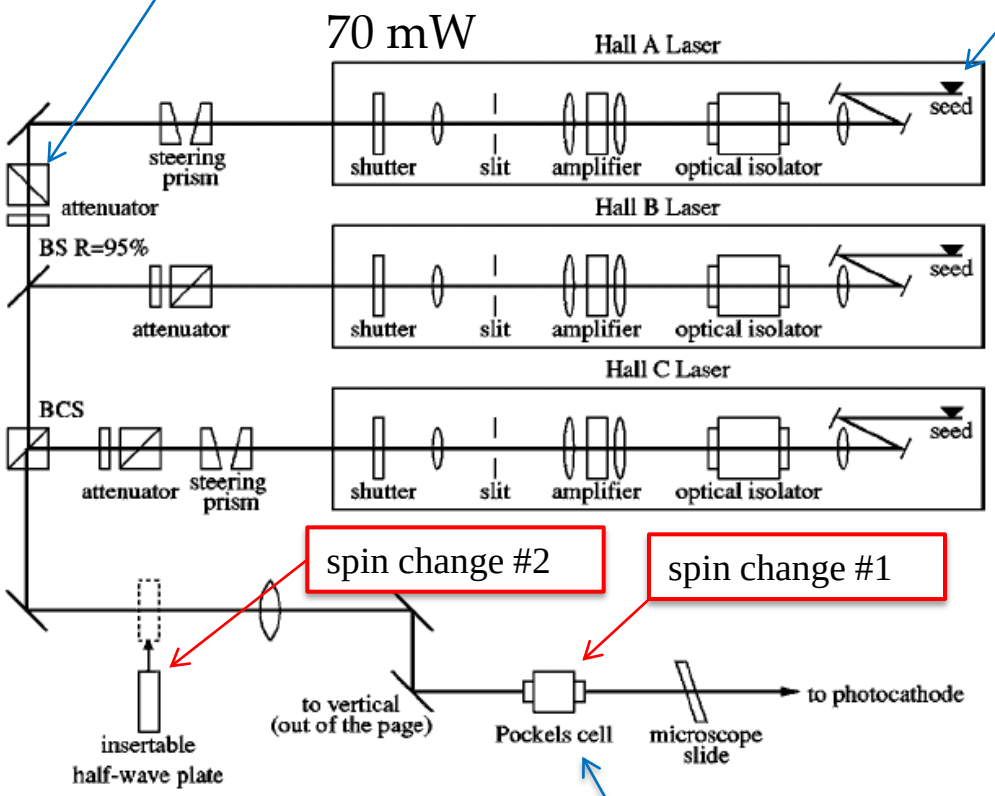

Change Linear Pol Axis by 90 deg.

Linear → Circular Pol. L&R switch

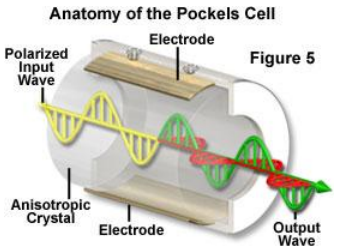

±λ/4 retardation
± 2.5 keV

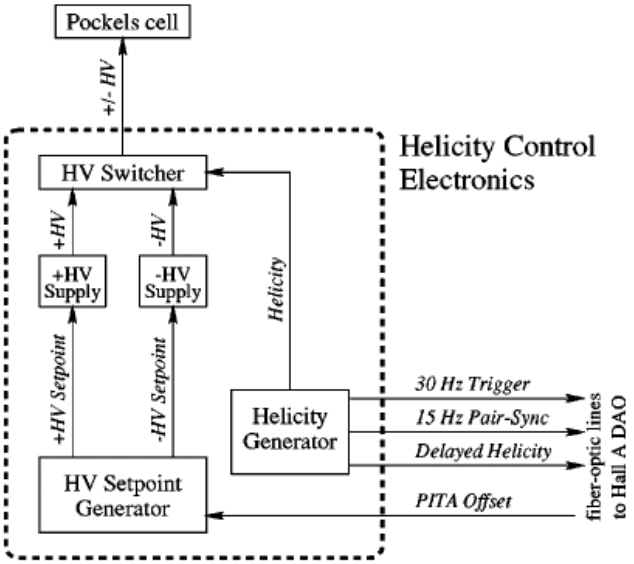

FIG. 3. Schematic diagram of the helicity control electronics. The *helicity* signal drives the high voltage on the Pockels cell. The system is electrically isolated from the rest of the lab (dashed box).

K.A. Aniol et al., PRC**69**, 065501 (2004)

Helicity Window

helicity control electronics (with Pockels cell)

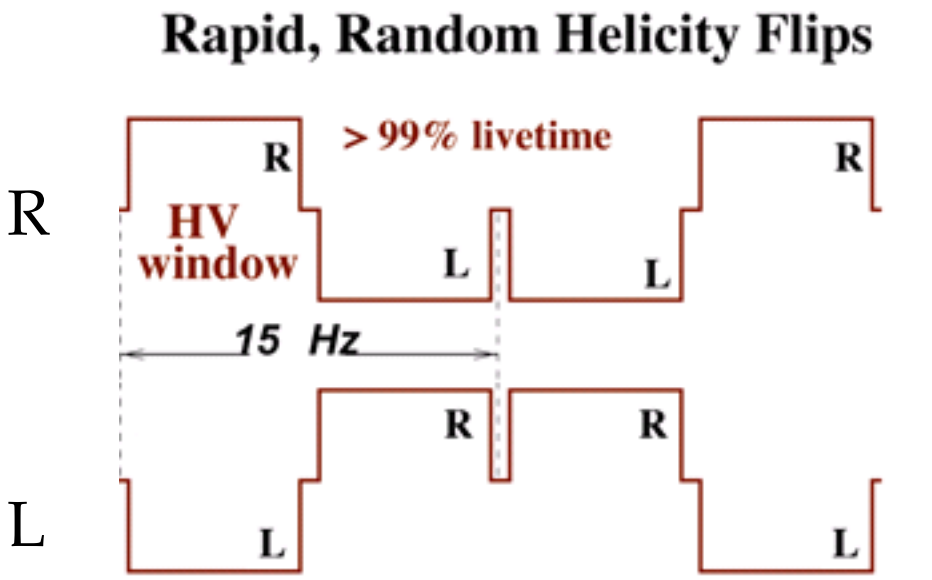

Helicity window pair (window quadruplet in PRL2012) R or L is chosen by a pseudo-random generator.

According to PRL2012, HV window is 8.33 msec (120Hz), thus window quadruplet 33.3 msec (30Hz), i.e. four times faster than the left figure.

Synchronized with the 60 Hz line frequency.

Signal transmission by fiber-optic cable: suppression of the ground noise and cross talk.

2×10^7 window quadruplets were recorded in PREX.

Pol. Electron Source (strained GaAs)

Photo-cathode, optical pumping

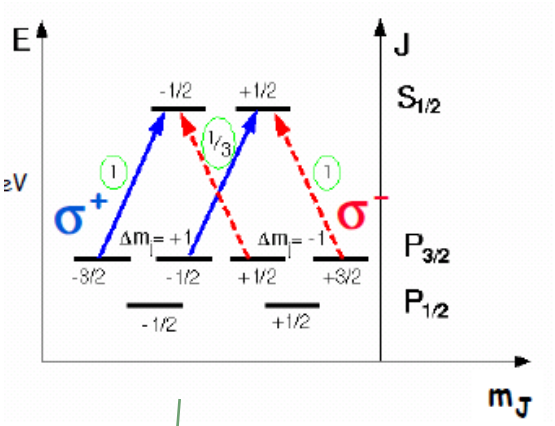

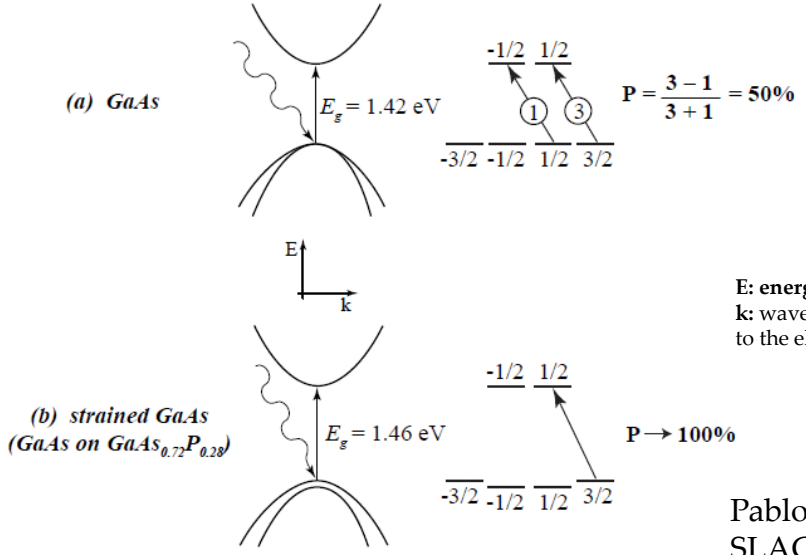

E: energy
k: wave vector perpendicular to the electric field

Pablo J. Sáez, SLAC-R-501, UC-414

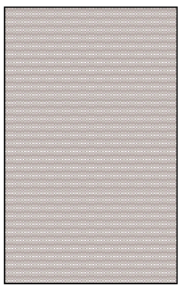

High QE ~ 20%
Pol ~ 35%

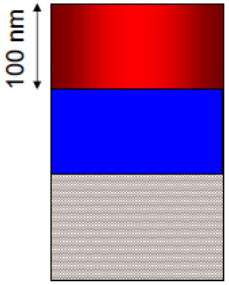

"conventional" material
QE ~ 0.2%
Pol ~ 75%
@ 850 nm

(PREX ex.)

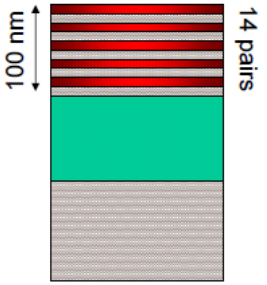

No strain relaxation
QE ~ 1.0 %
Pol ~ 85%
@ 780 nm

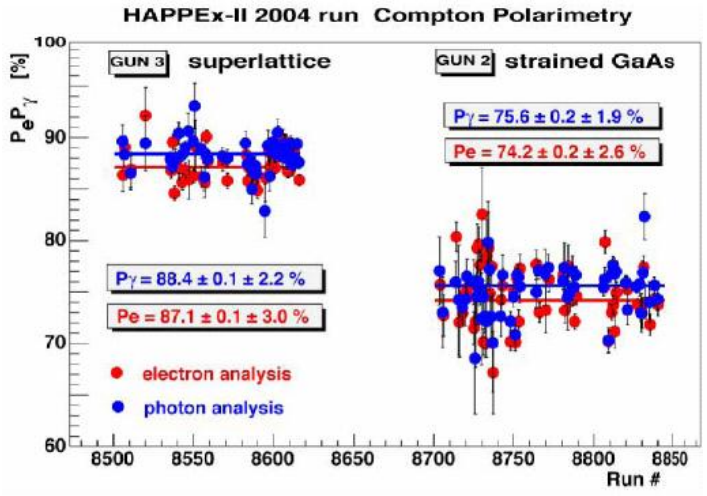

GaAs and GaAsP have a lattice mismatch.

J. Grames

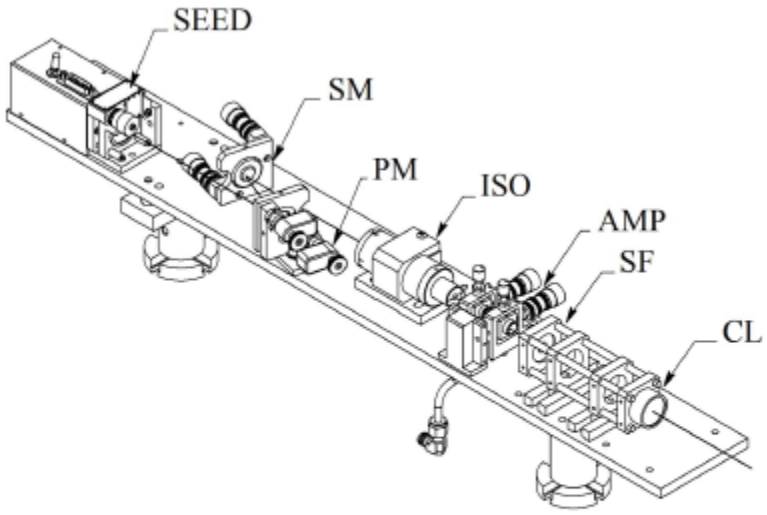

FIG. 6. The MOPA gain-switched diode seed laser and diode amplifier system: SM, steering mirror; PM, picomotor; ISO, optical isolator; AMP, single pass diode amplifier; SF, spatial filter; CL, cylindrical lens.

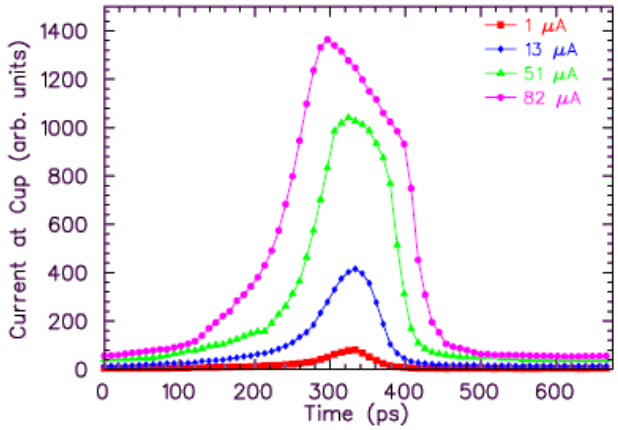

FIG. 7. (Color) Electron bunch length plots at the chopper slits at four different beam currents, obtained from a bulk GaAs cathode in the first polarized electron source. The observed bunch lengthening at higher current led to the installation of a 1497 MHz prebuncher between the gun and the injector chopper.

spin change #3

Wien-Filter with Solenoids

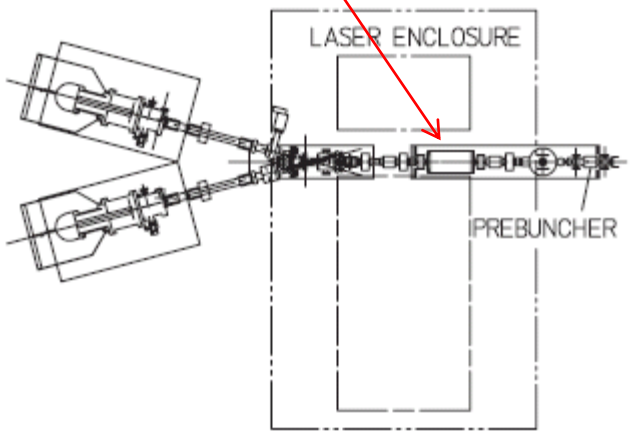

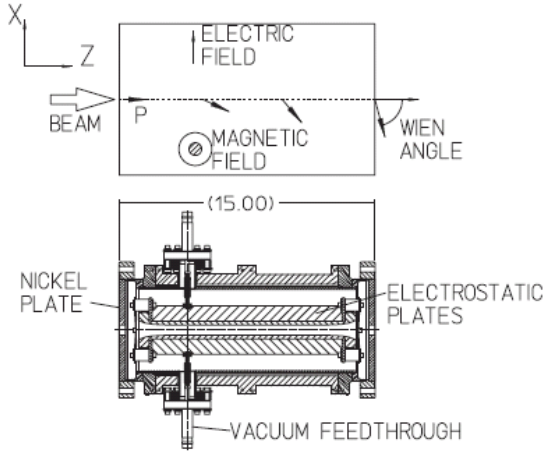

FIG. 4. The Wien filter spin manipulator used with CEBAF's second and third polarized electron sources. The magnet is not shown in the cutaway view.

Double Wien Filter

Crossed E & B fields to rotate the spin

- Two Wien Spin Manipulators in series
- Solenoid rotates spin +/-90 degrees (spin rotation as B but focus as B^2).

Flips spin without moving the beam !

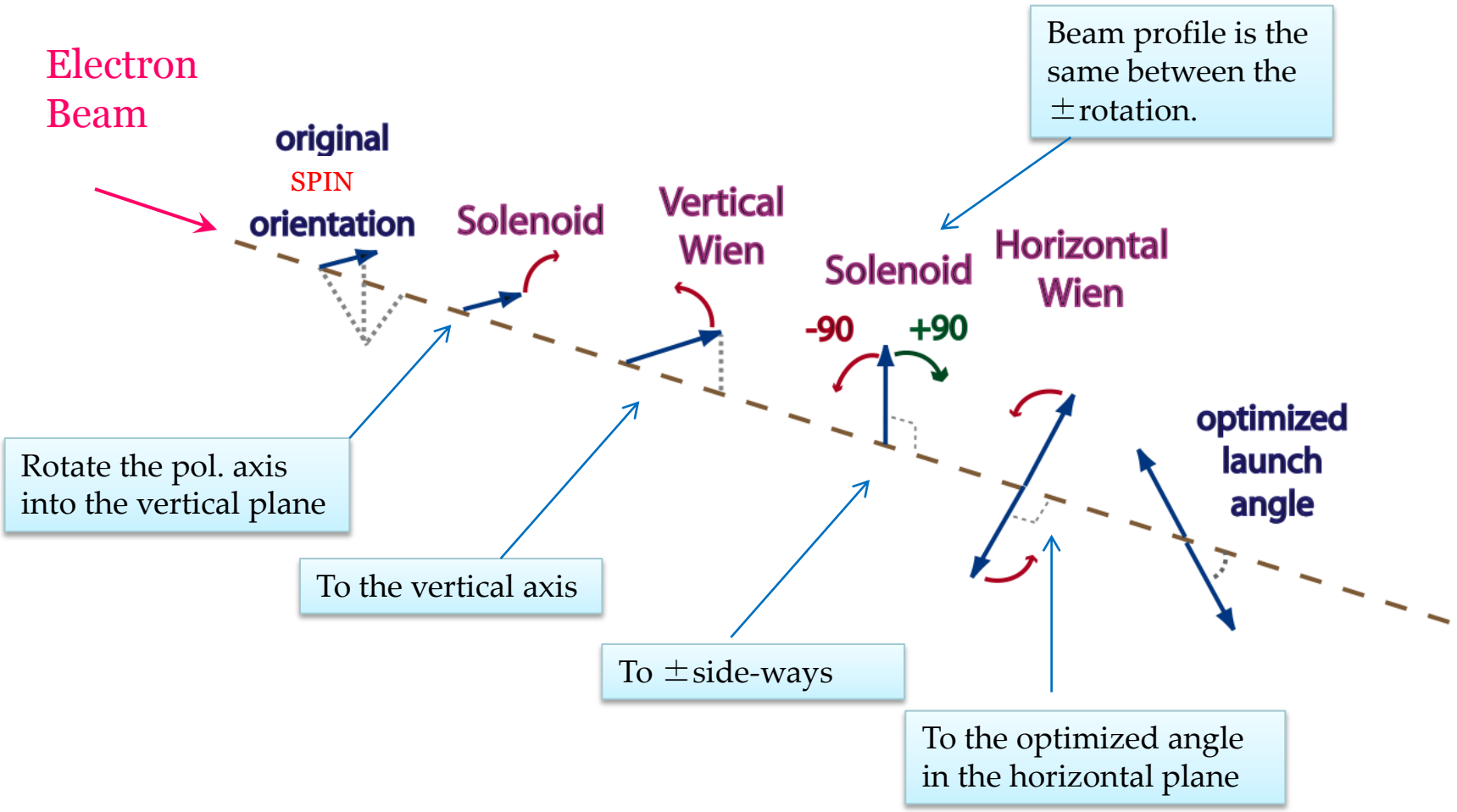

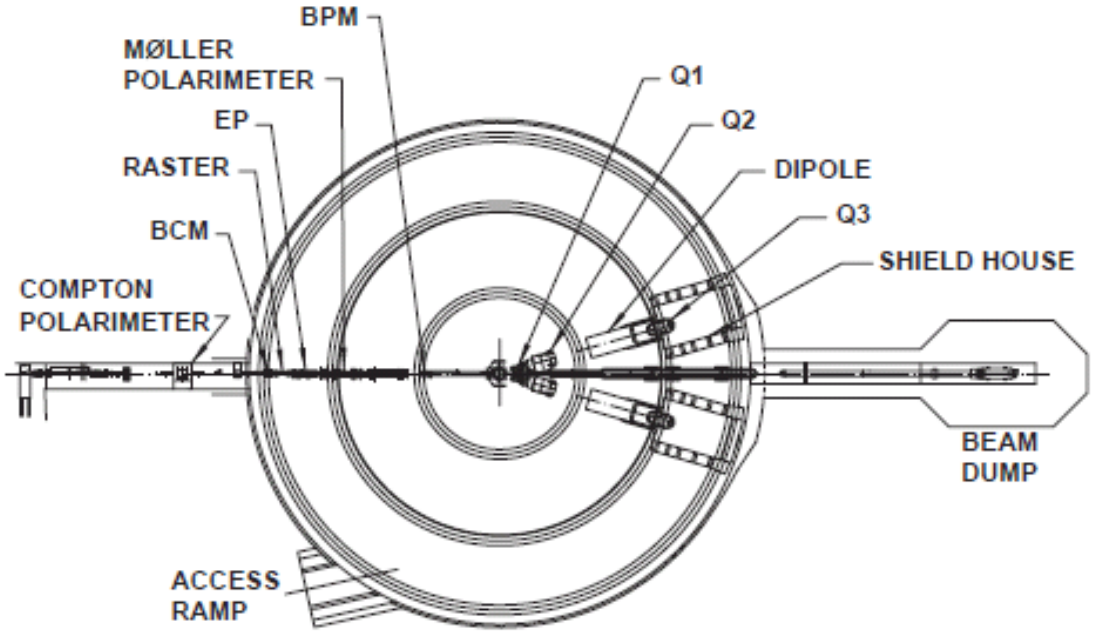

Fig. 18. Schematic layout of Hall A, indicating the location of the Compton and the Møller polarimeters, the raster, the EP energy measurement system, the beam current monitors (BCM) and the beam position monitors (BPM) upstream of the target. Also indicated are the locations of the components of one of the high-resolution spectrometers (Q1, Q2, dipole, Q3 and shield house) and of the beam dump and the truck access ramp.

[34] J. Alcorn et al., NIMA522, 294(2004)

Thin-Wire Beam Position Monitor (BPM)

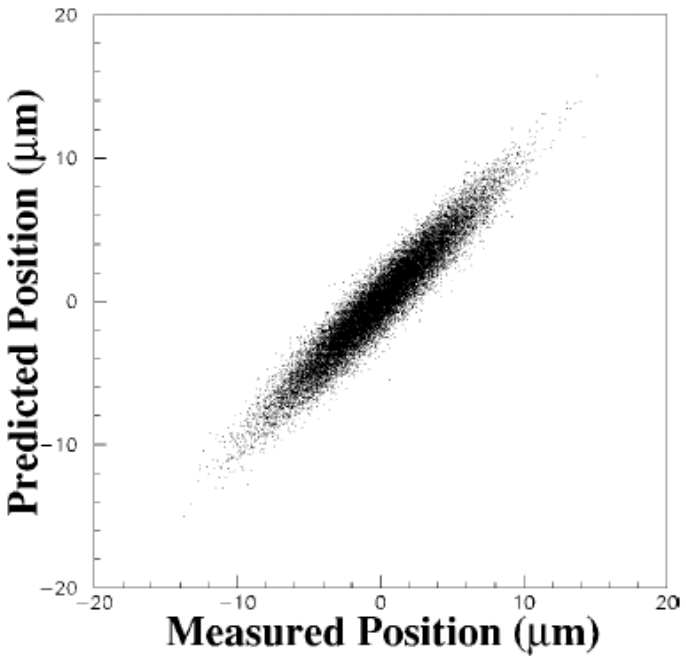

FIG. 5. Window-to-window beam jitter as measured by a BPM is plotted along the *x* axis. On the *y* axis is plotted the beam position as predicted by nearby BPMs. The residuals are smaller than 1 μm.

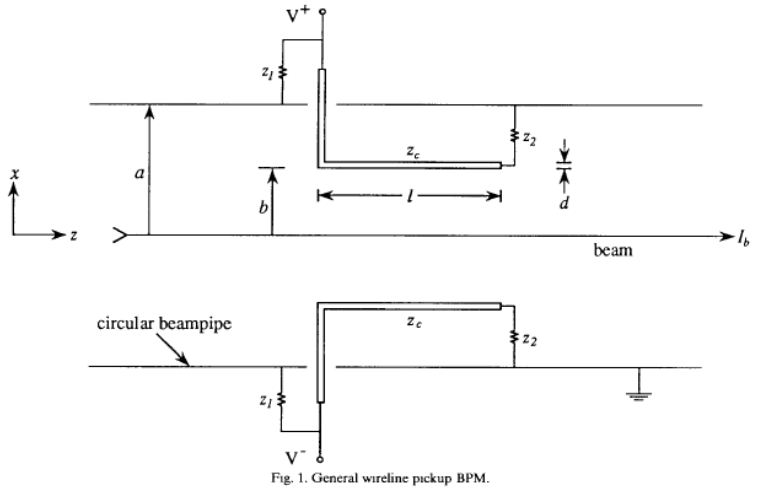

Fig. 1. General wireline pickup BPM.

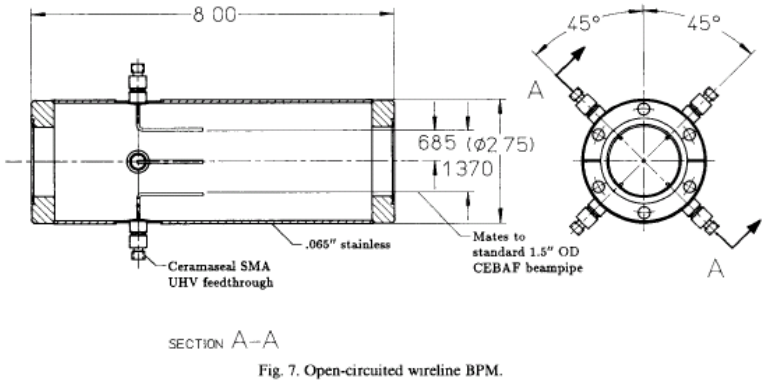

Fig. 7. Open-circuited wireline BPM.

$\Delta X \sim 1\mu m$

1-10 μm fluctuation in $\sigma(\Delta X)$

5 BPMs are placed in the beam line recorded in every 1Hz

[34] J. Alcorn et al., NIMA522,294(2004)

W. Barry., NIMA301_407(1991)

Beam Current Monitor (BCM)

Two RF cavity monitors (non-destructive)

stainless steel, cylindrical, high-Q (3000) wave guide (1.497 GHz)

high-precision 16bit ADC, non-linearity < 0.1%

Precision: 4×10^{-5} at 100 μA for a 30 msec beam window

"Unser monitor" for absolute beam current
not important for HAPPEX (and PREX)

toroidal Paramagnetic Current Transformer (PCT)
sensitive to the DC component of the magnetic field generated by the beam current around the beam pipe

see https://www.jlab.org/div_dept/admin/publications/papers/01/ACT01-12.pdf

[34] J. Alcorn et al., NIMA522,294(2004)

Beam Polarimeter (Compton Polarimeter)

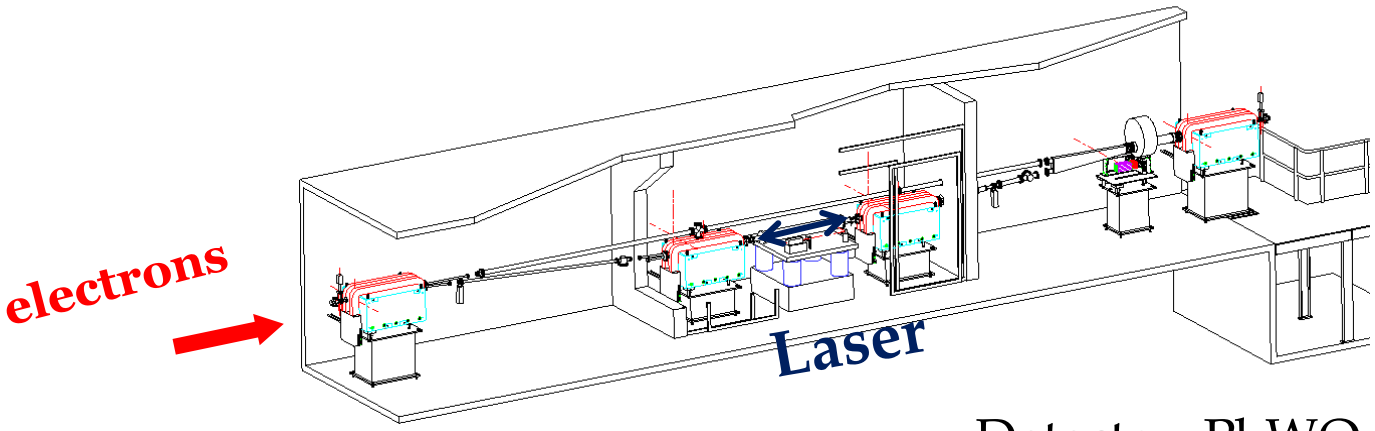

$\vec{e} - \vec{\gamma}$ *scattering*

Detector: $PbWO_4$ crystals

Green Laser
(increased sensitivity at low E)
Integrating Method
(removes some systematics of analyzing power)

Upgrade for 1% accuracy at 1 GeV

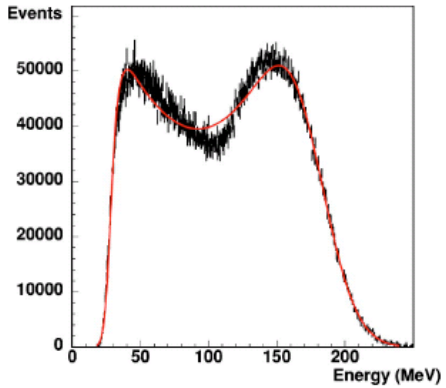

FIG. 13. (Color online) Compton spectrum as measured by the photon calorimeter. The curve is a fit of the Compton cross section convoluted with a Gaussian resolution of the calorimeter [see Eq. (20)].

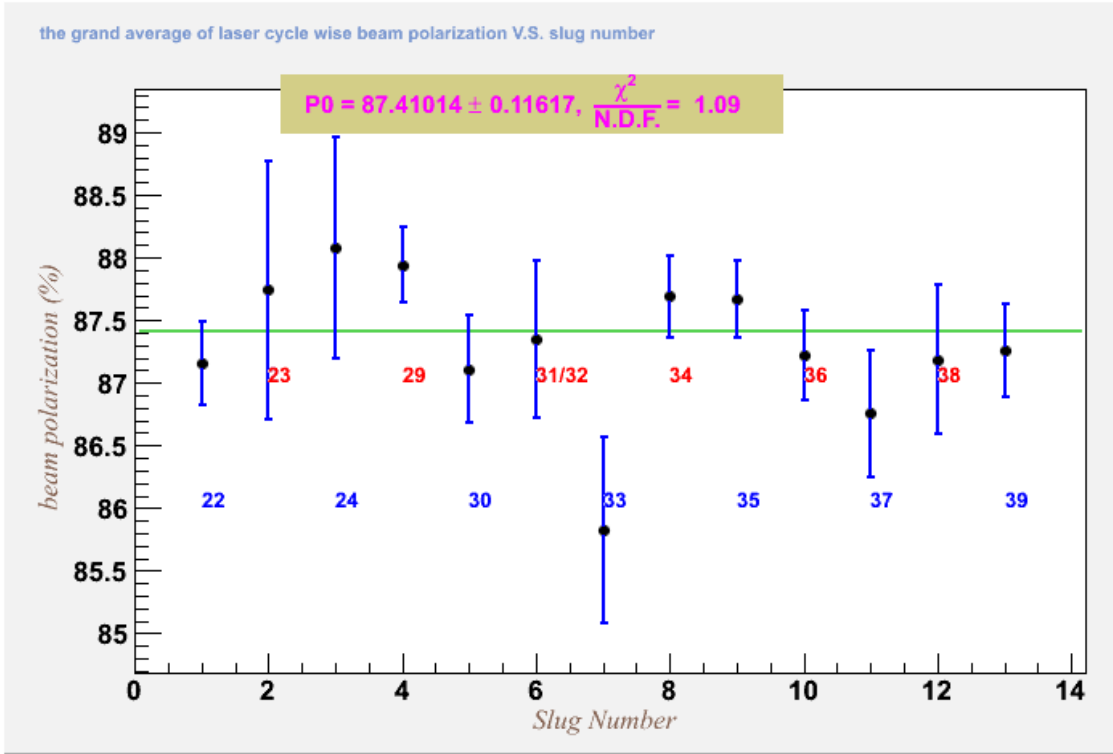

Magnet and Target

Upgraded for PREX

Moller Polarimeter

$\vec{e} - \vec{e}$ *scattering*

Superconducting Magnet from Hall C

Saturated Iron Foil Targets (at 4 T)

1 % Accuracy in Polarization

$$A_m^{exp} = \sum_{i=X,Y,Z} (A_{mi}^{th} \cdot P_i^{targ} \cdot P_i^{beam}), \qquad (17)$$

$$A_{mZ}^{th} = -\frac{\sin^2\theta_{c.m.}(7+\cos^2\theta_{c.m.})}{(3+\cos^2\theta_{c.m.})^2}. \qquad (18)$$

ferromagnetic foil

$P^{targ} = 7.95 \pm 0.24$ % at 24 mT

$75^\circ < \vartheta_{c.m.} < 105^\circ$

$-5^\circ < \phi_{c.m.} < 5^\circ$

The values are before PREX meas.

[34] J. Alcorn et al., NIMA522, 294(2004)

Lead / Diamond Target

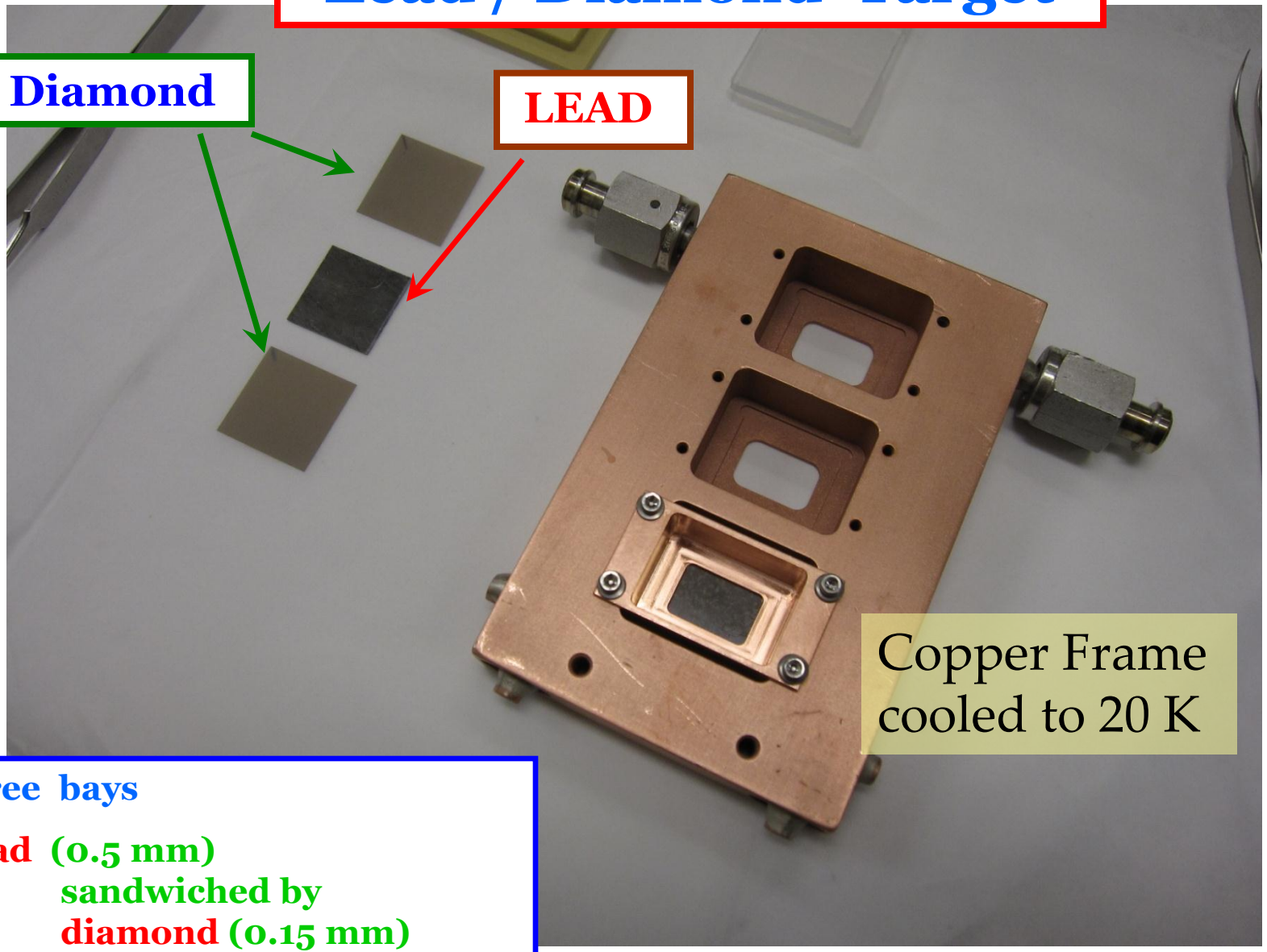

- Three bays
- Lead (0.5 mm)
  sandwiched by
  diamond (0.15 mm)
- Liquid He cooling (30 Watts)

Performance of Lead / Diamond Targets

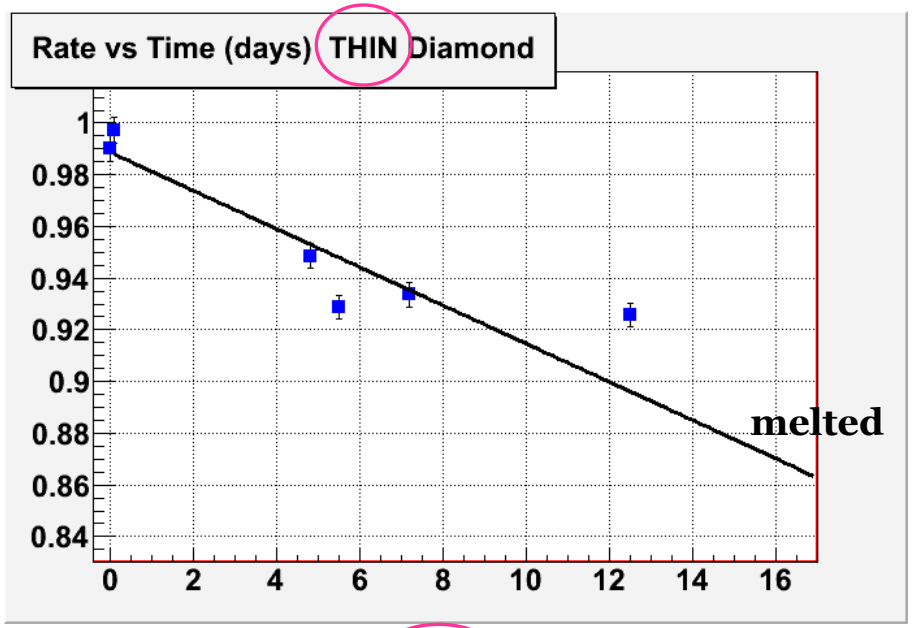

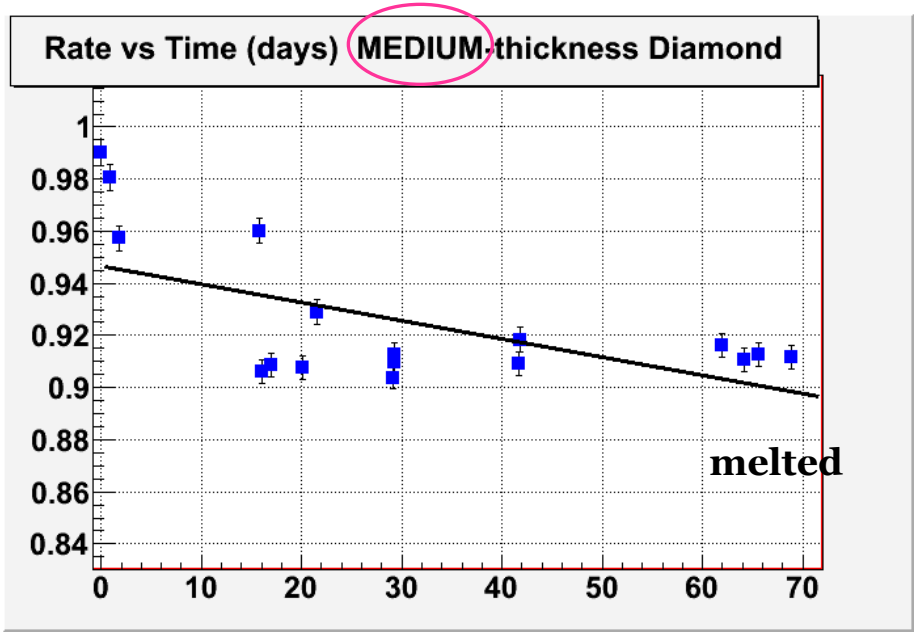

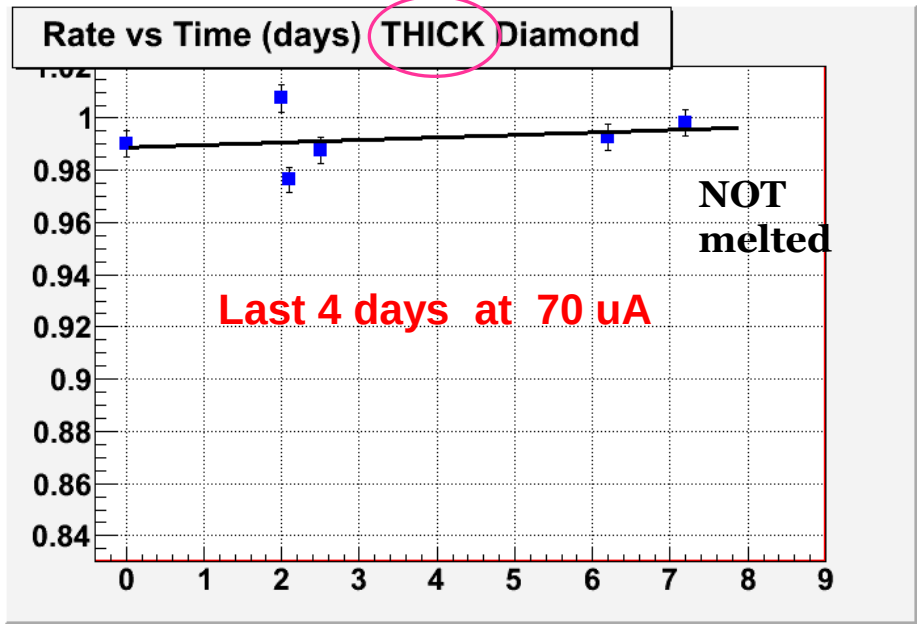

Targets with thin diamond backing (4.5 % background) degraded fastest.

Thick diamond (8%) ran well and did not melt at 70 uA.

→ Solution: Run with 10 targets.

High-Resolution Spectrometers (HRSs)

placed at $\vartheta_{lab} = 5^{\circ}$

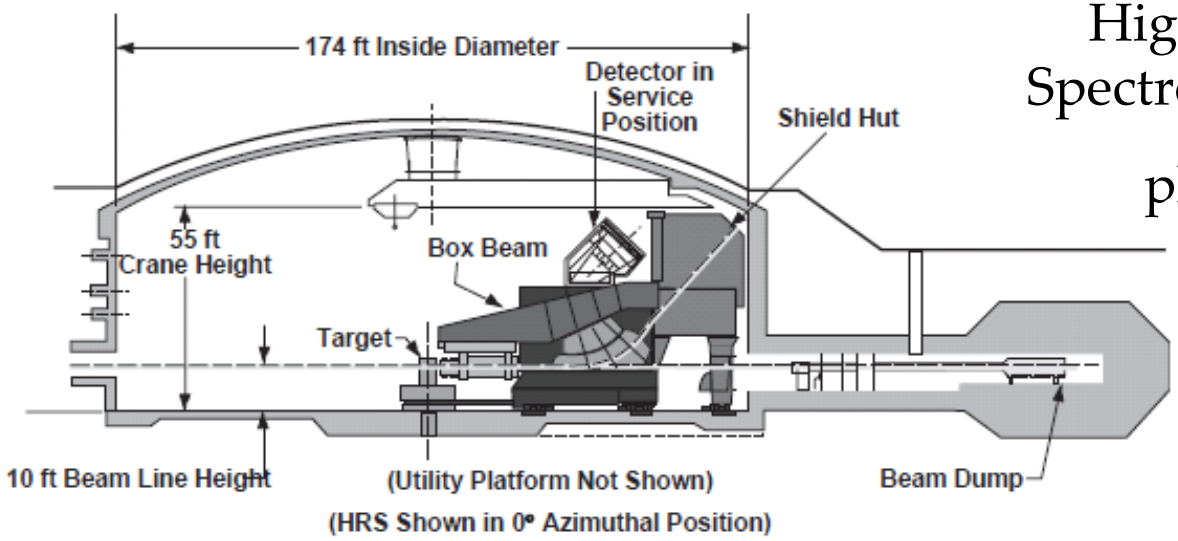

Fig. 2. Schematic cross section of Hall A with one of the HRS spectrometers in the (fictitious) 0° position.

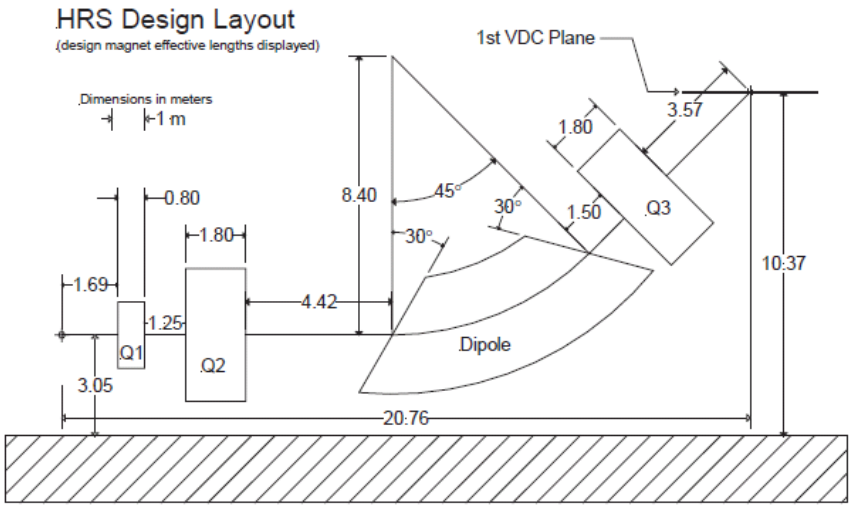

Fig. 5. Schematic layout of a HRS device, showing the geometrical configuration of the three quadrupole and the dip shown is the location of the first VDC tracking detector.

Main design characteristics of the Hall A high resolution spectrometers; the resolution values are for the FWHM

Configuration	QQD_nQ vertical bend
Bending angle	45°
Optical length	23.4 m
Momentum range	0.3–4.0 GeV/c
Momentum acceptance	$-4.5\% < \delta p/p < +4.5\%$
Momentum resolution	1×10^{-4}
Dispersion at the focus (D)	12.4 m
Radial linear magnification (M)	−2.5
D/M	5.0
Angular range	
HRS-L	12.5–150°
HRS-R	12.5–130°
Angular acceptance	
Horizontal	±30 mrad
Vertical	±60 mrad
Angular resolution	
Horizontal	0.5 mrad
Vertical	1.0 mrad
Solid angle at $\delta p/p = 0$, $y_0 = 0$	6 msr
Transverse length acceptance	±5 cm
Transverse position resolution	1 mm

[34] J. Alcorn et al., NIMA522, 294(2004)

Position sensitive detectors (VDCs)

only used for calibration purposes

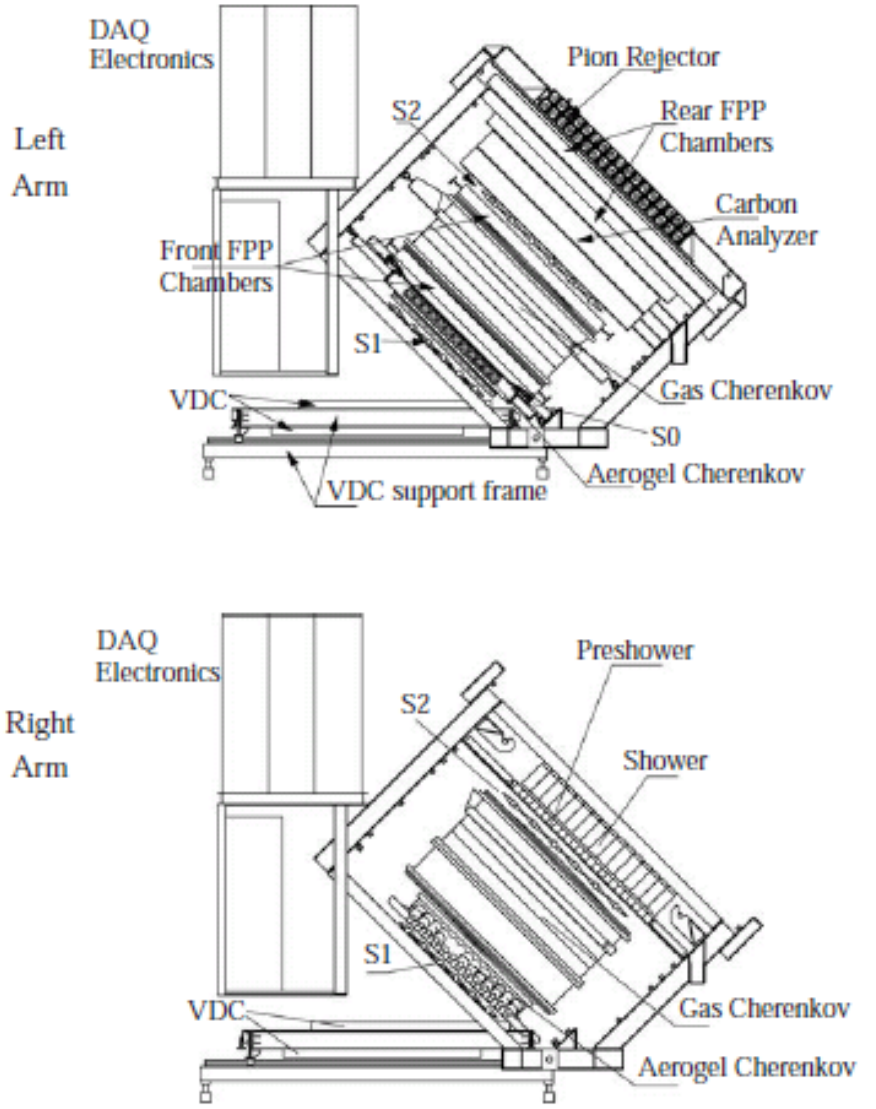

Fig. 8. Sideview of detector stack, shown in the top (bottom) figure for the left (right) (w.r.t. the beam line) HRS device. Individual elements of the detector system are indicated in the configuration used most frequently. Also shown is the position of the data-acquisition (DAQ) electronics and of the VDC support frame.

[34] J. Alcorn et al., NIMA522, 294(2004)

Integrated Detectors

quartz detector
Cherenkov light
PMT (quartz window)

Stability of the PMT signal?

The fluctuations of the L-R difference for each window is dominated by the counting statistics up to 1 GHz

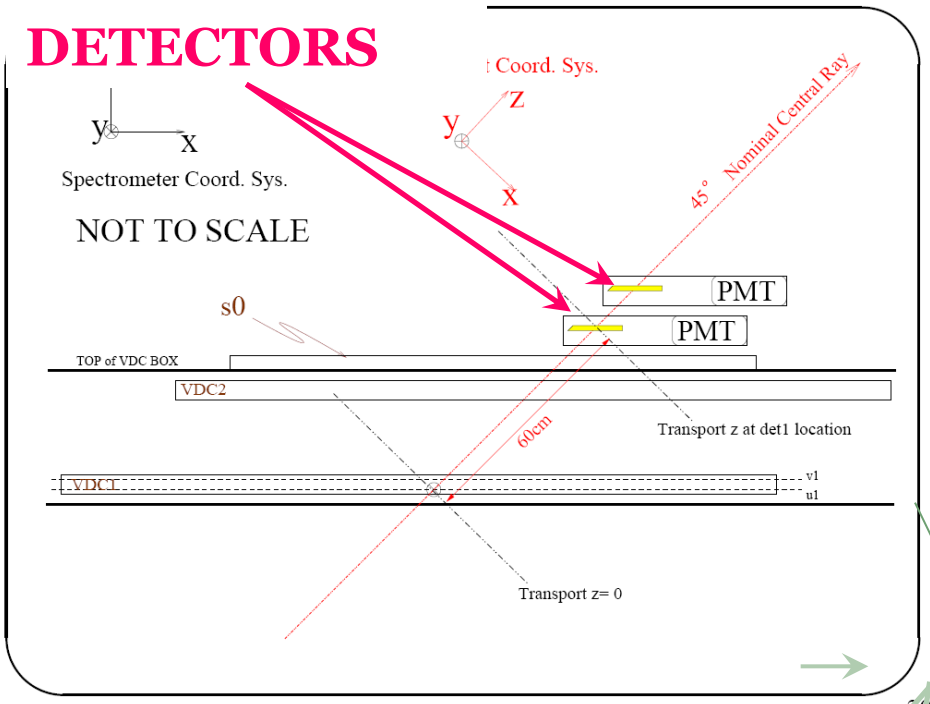

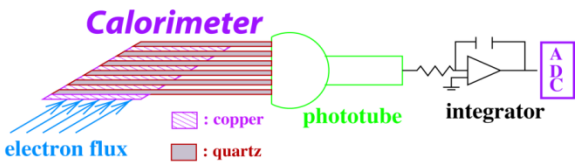

850 MHz

The ^{208}Pb 1st Ex. state is negligible.

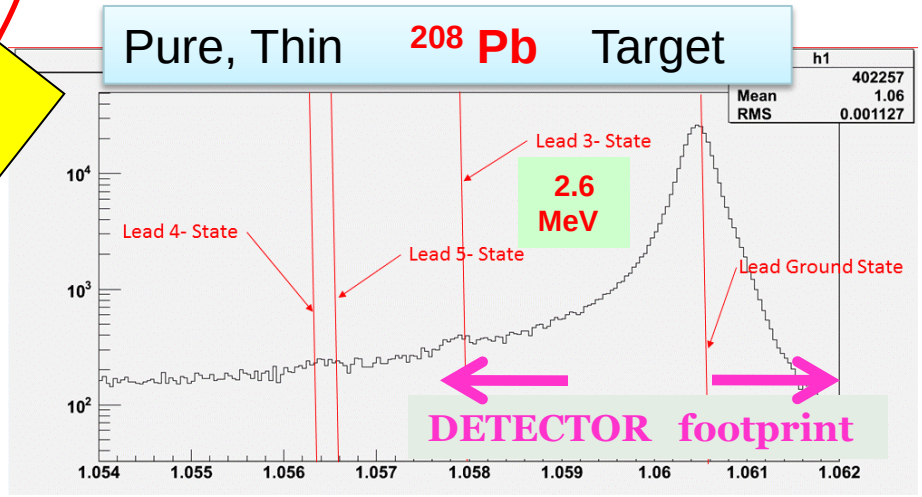

Important Systematic : **P I T A Effect**

Polarization Induced Transport Asymmetry

Intensity Asymmetry $A_I = \varepsilon \, \Delta \sin(\theta)$

where $\varepsilon = \dfrac{T_x - T_y}{T_x + T_y}$

Transport Asymmetry

Laser at Pol. Source

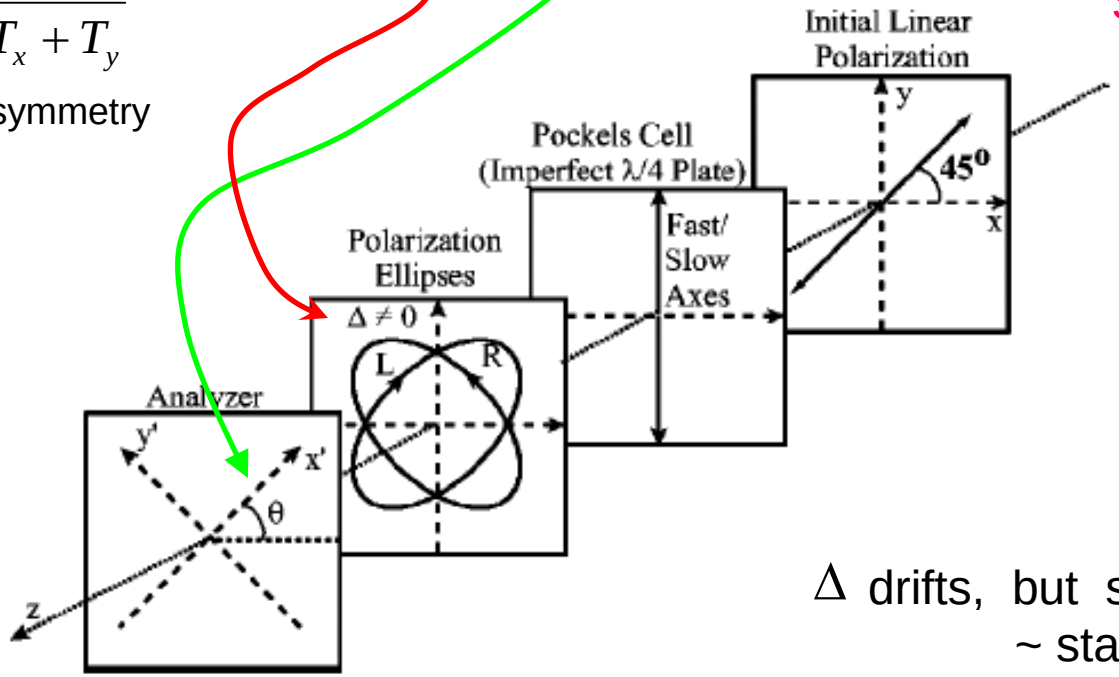

Δ drifts, but slope is ~ stable.

$\Longrightarrow$ Feedback on Δ

99.99% circular pol. but with 1.4% linear pol. (different orientation) causes intensity asymmetry

Intensity Feedback

Adjustments for small phase shifts to make close to circular polarization

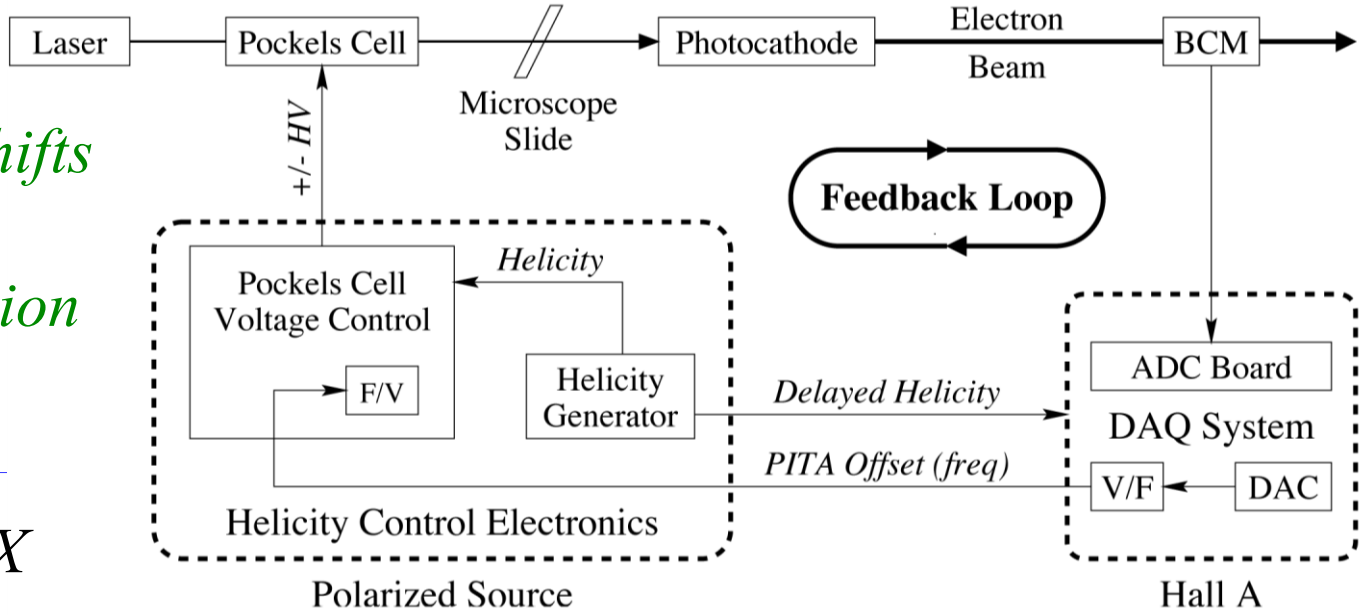

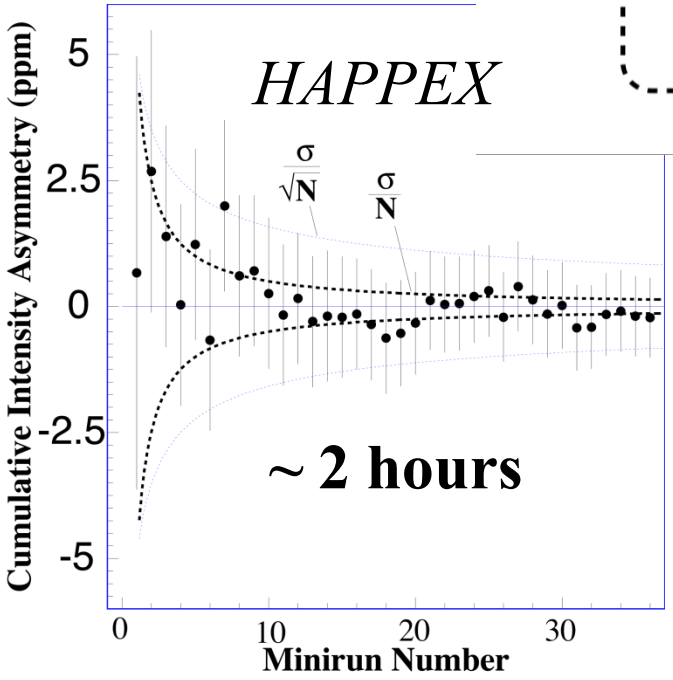

Low jitter and high accuracy allows sub-ppm Cumulative charge asymmetry in ~ 1 hour

In practice, aim for 0.1 ppm over duration of data-taking.

Transverse Polarization

Part I: Left/Right Asymmetry

Transverse Asymmetry

$$A_T \approx A_T^0 \; P_T \; \sin\phi$$

Theory est. (Afanasev)

$$A_T^0 = 5 \pm 1 \quad ppm$$

Transverse polarization

$$P_T = P \sin\theta \qquad \theta \leq 3^o$$

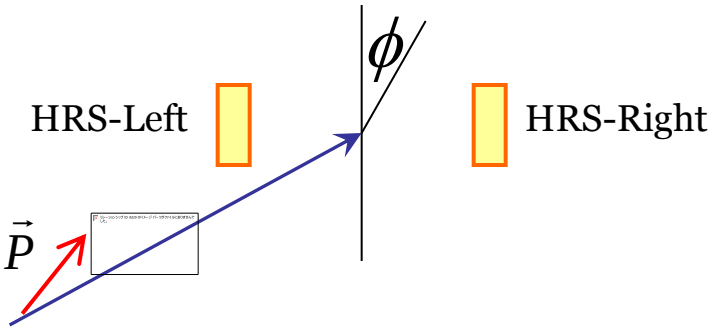

Systematic Error for Parity

$$\rightarrow \quad \delta A = \delta\left(A_T^0 \; \xi \; P_T\right)$$

"Error in"

ξ = Left-right apparatus asymmetry

Control θ w/ slow feedback on polarized source solenoids.

$\delta A_T^0 = \pm 1 \quad ppm$ measure in ~ 1 hr (+ 8 hr setup)

Need $\xi \; P_T \ll 10^{-3} \pm 10^{-3}$

correction — syst. err.

Transverse Polarization

Part II: Up/Down Asymmetry

Vertical misalignment

Horizontal polarization
e.g. from (g-2)

$$< \cos\phi > \neq 0 \quad \rightarrow$$

$$P_T = P \sin\theta$$

up/down misalignment

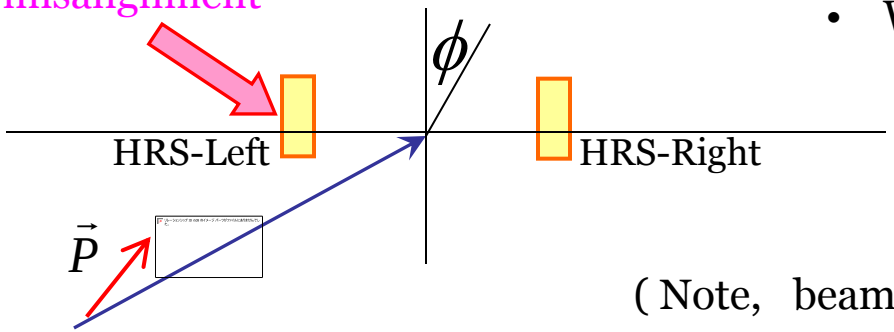

Systematic Error for Parity

$$\delta A = \delta\left(A_T^0 \; P_T \; < \cos\phi >\right)$$

- Measured in situ using 2-piece detector.
- Study alignment with tracking & M.C.
- Wien angle feedback (θ)

Need

$$P_T \; < \cos\phi > \; \ll \; 10^{-3} \; \pm 10^{-3}$$

(Note, beam width is very tiny $\sim 100\ \mu m$)

page-3

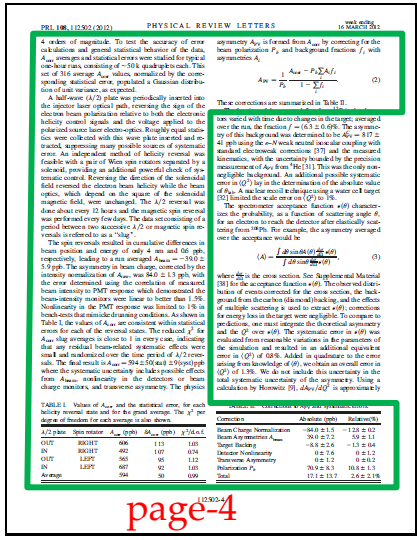

page-4

Analysis Details, Calibrations, Corrections

Correction/Uncertainty of the Asymmetry

$$A_{corr} = A_{raw} - A_Q - (\alpha\Delta_E + \Sigma\beta_i\Delta x_i)$$

- A_{corr}: corrected asymmetry
- A_{raw}: raw data asymmetry
- A_Q: beam intensity fluctuation
- A_{beam}

Beam jitter in window quadruplets:
ΔE/E~2 ppm
Δ X~20 μm

monitored and converted to A and be corrected as A_{beam}.

Coefficients are measured several times each hour with modulation by steering coils and cavity

Slopes from
- **natural beam jitter (regression)**
- **beam modulation (dithering)**

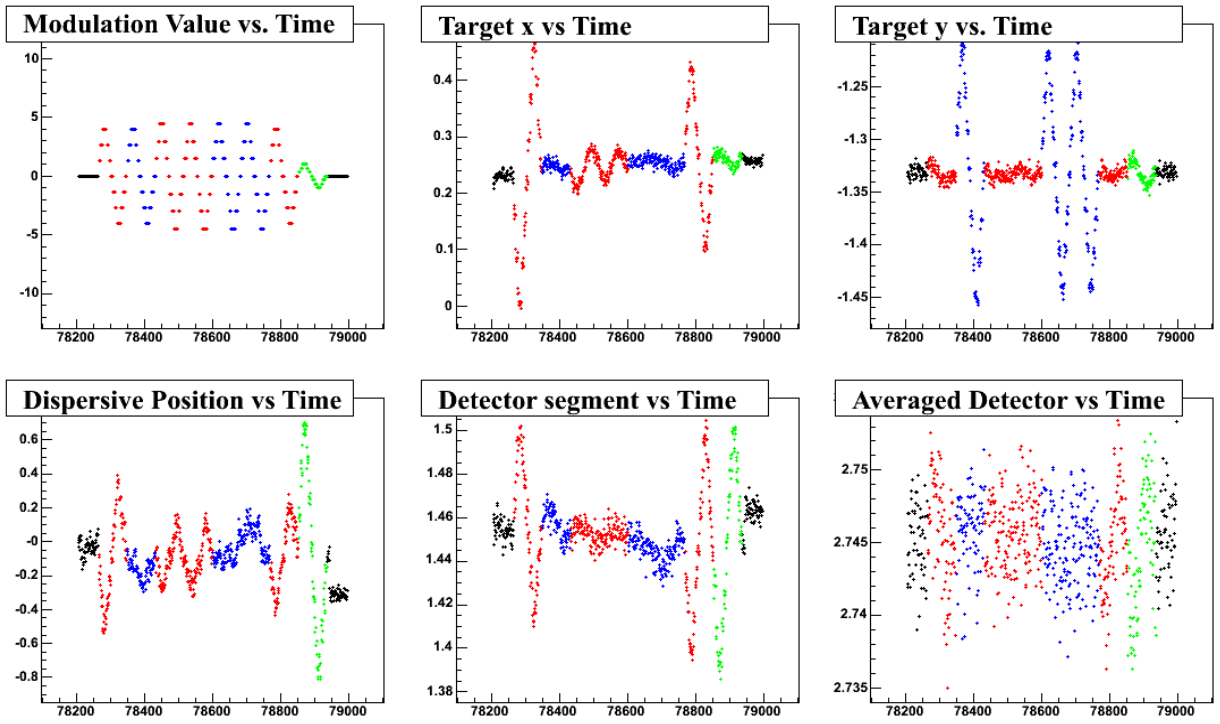

Correction/Uncertainty of the Asymmetry

$$A_{corr} = A_{raw} - A_Q - (\alpha\Delta_E + \Sigma\beta_i\Delta x_i)$$

- A_{corr}: corrected asymmetry
- A_{raw}: raw data
- A_Q: beam intensity fluctuation
- $\alpha\Delta_E + \Sigma\beta_i\Delta x_i$: A_{beam}

$A_{beam} = -39.0 \pm 5.9$ ppb

$A_Q = 84.0 \pm 1.3$ ppb

from the text

Why the numbers in Table II are different?

A_{raw} is not written

$A_{corr} = 594 \pm 50(stat) \pm 9(syst)$ ppb

from A_{beam}, detector non-linearlity, A_Q, and transverse asymmetry

Correction/Uncertainty of the Asymmetry

Spin change

#1 by Pockels cell: for every window (83 msec)

#2 by a $\lambda/2$ plate: for every 12 hours

#3 by a solenoid spin rotator: for every few days

With changing the spin by #2 and #3, the same results were obtained within the (statistical) uncertainty

The averaged result:

$$A_{corr} = 594 \pm 50(stat) \pm 9(syst)\ ppb$$

TABLE I. Values of A_{corr} and the statistical error, for each helicity reversal state and for the grand average. The χ^2 per degree of freedom for each average is also shown.

$\lambda/2$ plate	Spin rotator	A_{corr} (ppb)	δA_{corr} (ppb)	χ^2/d.o.f.
OUT	RIGHT	606	113	1.03
IN	RIGHT	492	107	0.74
OUT	LEFT	565	95	1.12
IN	LEFT	687	92	1.03
Average		594	50	0.99

Background, Beam Polarization

$$A_{\mathrm{PV}} = \frac{1}{P_b} \frac{A_{\mathrm{corr}} - P_b \sum_i A_i f_i}{1 - \sum_i f_i}. \qquad (2)$$

Background from carbon (diamond):
f = 6.3±0.6 %, A=817±41 ppb

by cal. using *e-N* weak neutral isoscalar coupling with corrections [37]

TABLE II. Corrections to A_{PV} and systematic errors.

Correction	Absolute (ppb)	Relative(%)
Beam Charge Normalization	-84.0 ± 1.5	-12.8 ± 0.2
Beam Asymmetries A_{beam}	39.0 ± 7.2	5.9 ± 1.1
Target Backing	-8.8 ± 2.6	-1.3 ± 0.4
Detector Nonlinearity	0 ± 7.6	0 ± 1.2
Transverse Asymmetry	0 ± 1.2	0 ± 0.2
Polarization P_b	70.9 ± 8.3	10.8 ± 1.3
Total	17.1 ± 13.7	$2.6 \pm 2.1\%$

Background, Beam Polarization

Beam Polarization

by Compton polarimeter (continuous)

P_b=88.2±0.1±1.0 %

by Moeller polarimeter (9 measurements)

P_b=90.3±0.1±1.1 %

Average of the two

P_b=89.2±1.0 %

TABLE II. Corrections to A_{PV} and systematic errors.

Correction	Absolute (ppb)	Relative(%)
Beam Charge Normalization	-84.0 ± 1.5	-12.8 ± 0.2
Beam Asymmetries A_{beam}	39.0 ± 7.2	5.9 ± 1.1
Target Backing	-8.8 ± 2.6	-1.3 ± 0.4
Detector Nonlinearity	0 ± 7.6	0 ± 1.2
Transverse Asymmetry	0 ± 1.2	0 ± 0.2
Polarization P_b	70.9 ± 8.3	10.8 ± 1.3
Total	17.1 ± 13.7	$2.6 \pm 2.1\%$

Background, Beam Polarization

Result after all the corrections

$$A_{\mathrm{PV}}^{\mathrm{Pb}} = 656 \pm 60(\mathrm{stat}) \pm 14(\mathrm{syst})\ \mathrm{ppb},$$

Scattering Angle, Acceptance

Scattering Angle Calibration

$\Delta\langle Q^2\rangle/\langle Q^2\rangle = 1\%$

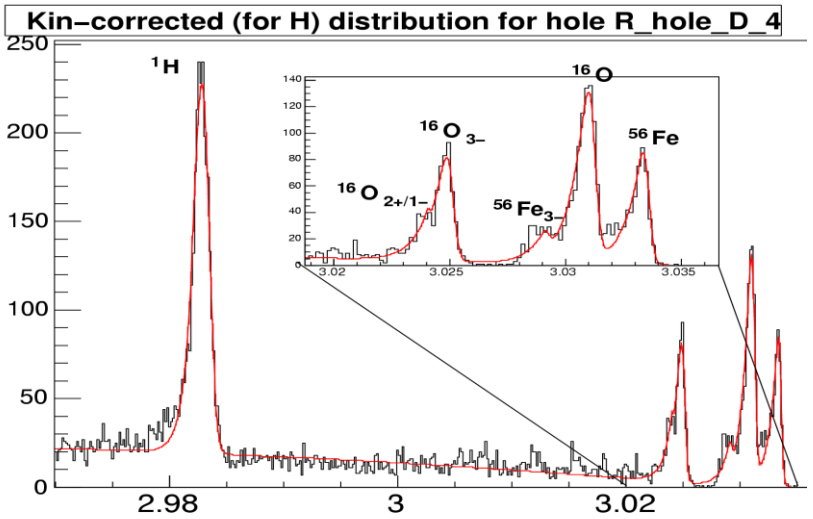

water cell target

Acceptance Averaging

$$\langle A\rangle = \frac{\int d\theta \sin\theta A(\theta)\frac{d\sigma}{d\Omega}\epsilon(\theta)}{\int d\theta \sin\theta \frac{d\sigma}{d\Omega}\epsilon(\theta)}, \qquad (3)$$

$\Delta\langle Q^2\rangle/\langle Q^2\rangle = 0.8\%$

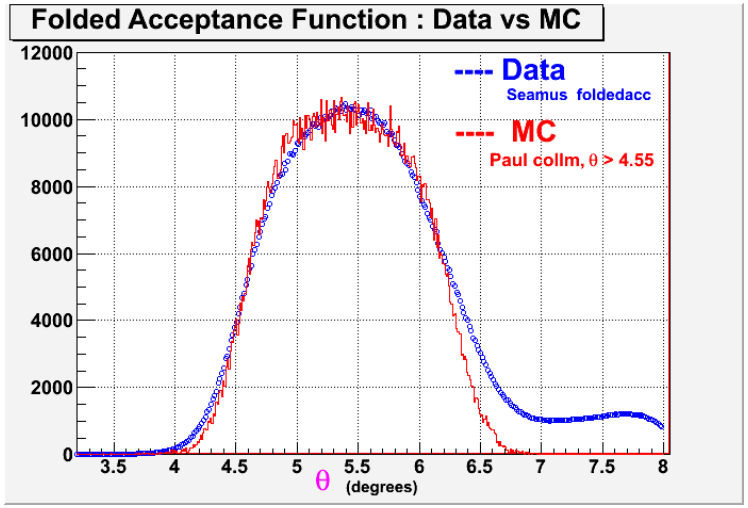

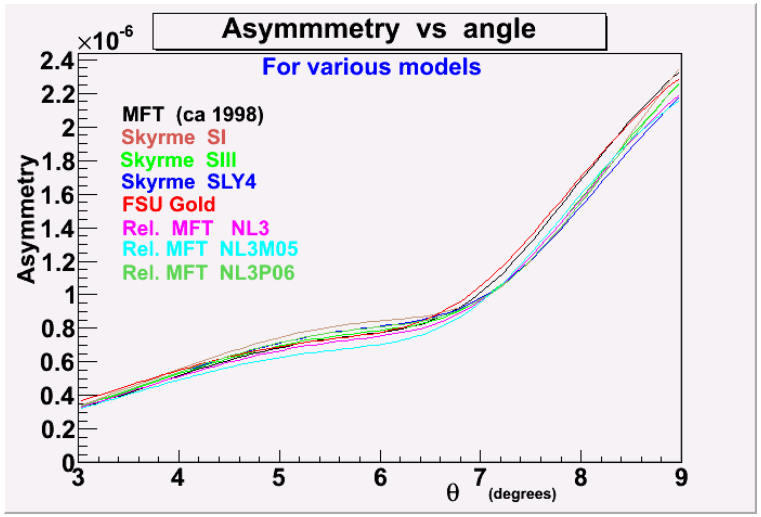

Result

Result after all the corrections

$$A_{PV}^{Pb} = 656 \pm 60(stat) \pm 14(syst)\ ppb,$$

$$\langle Q^2 \rangle = 0.008\,80 \pm 0.000\,11\ GeV^2$$

$q=\langle Q^2\rangle^{1/2}=0.475\pm0.003\ fm^{-1}$

Result

$$R_n = 5.78^{+0.16}_{-0.18}$$

$$R_n - R_p = 0.33^{+0.16}_{-0.18}\ \text{fm}$$

In abstract

"provides the first electroweak observation of the neutron skin"

In summary

"A future run is planned which will reduce the quoted uncertainty by a factor of 3 [43], to discriminate between models and allow predictions relevant for the description of neutron stars and parity violation in atomic systems."

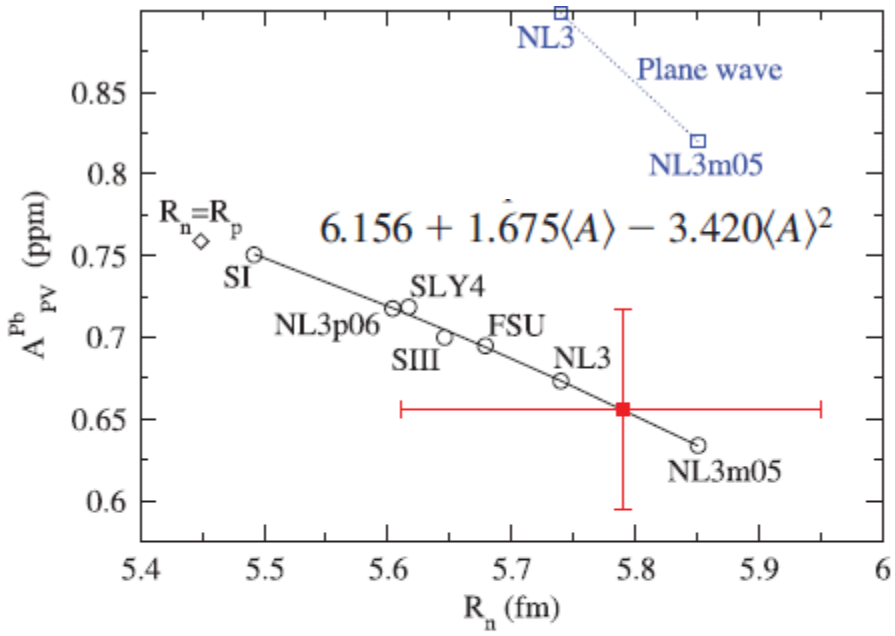

FIG. 1 (color). Result of this experiment (red square) vs neutron point radius R_n in 208Pb. Distorted-wave calculations for seven mean-field neutron densities are circles while the diamond marks the expectation for $R_n = R_p$[39]. References: NL3m05, NL3, and NL3p06 from [11], FSU from [12], SIII from [13], SLY4 from [14], SI from [15]. The blue squares show plane wave impulse approximation results.

No discussion on the impact of the result?

Is this analysis really model independent?

Science

Physicists Measure the Skin of a Nucleus

by Adrian Cho on 2 March 2012

Science Now

...

Nailing down such parameters would have equally big implications for the theory of neutron stars, says James Lattimer, a theoretical astrophysicist at Stony Brook University in New York state. "That directly tells you the radius of a neutron star [of a given mass] and a lot of other things like the thickness of its crust, the response of its surface to explosions, et cetera," Lattimer says.

Alas, the uncertainty on the PREX measurement is still too large to pin down the parameters, Lattimer says. "It's a very important experiment and has the potential to constrain theory very nicely, but it's not there yet," he says. JLab's Michaels says the PREX team will run the experiment next year and aims to reduce the uncertainty to one-third its current value. "Then it becomes a very interesting result," he says.

Something else physicists will be watching for: The PREX measurement suggests that the neutron skin of lead-208 is twice as thick as more-precise but model-dependent methods indicate. Right now, the PREX result has too much uncertainty to pose a direct challenge to earlier estimates. But if the new value holds up as the uncertainty shrinks, things could get really interesting, Nazarewicz says: "Then, there is something wrong with all theoretical models." There's a possibility to set your skin a-tingling.

Determination of Symmetry Energy

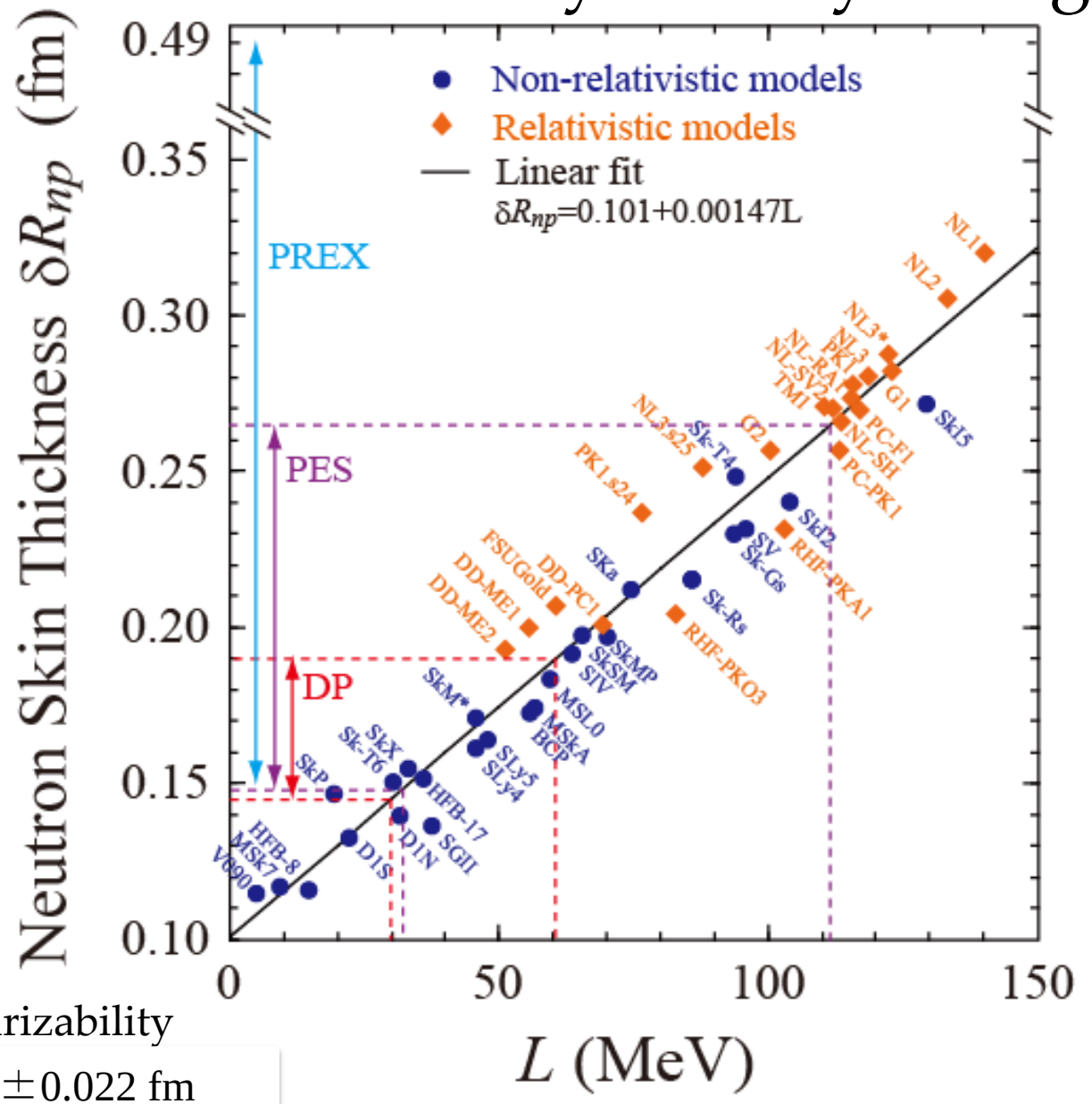

DP: Dipole Polarizability

R_n-R_p = 0.168±0.022 fm

Based on the work by X. Roca-Maza *et al.*, PRL**106**, 252501 (2011)

Determination of Symmetry Energy

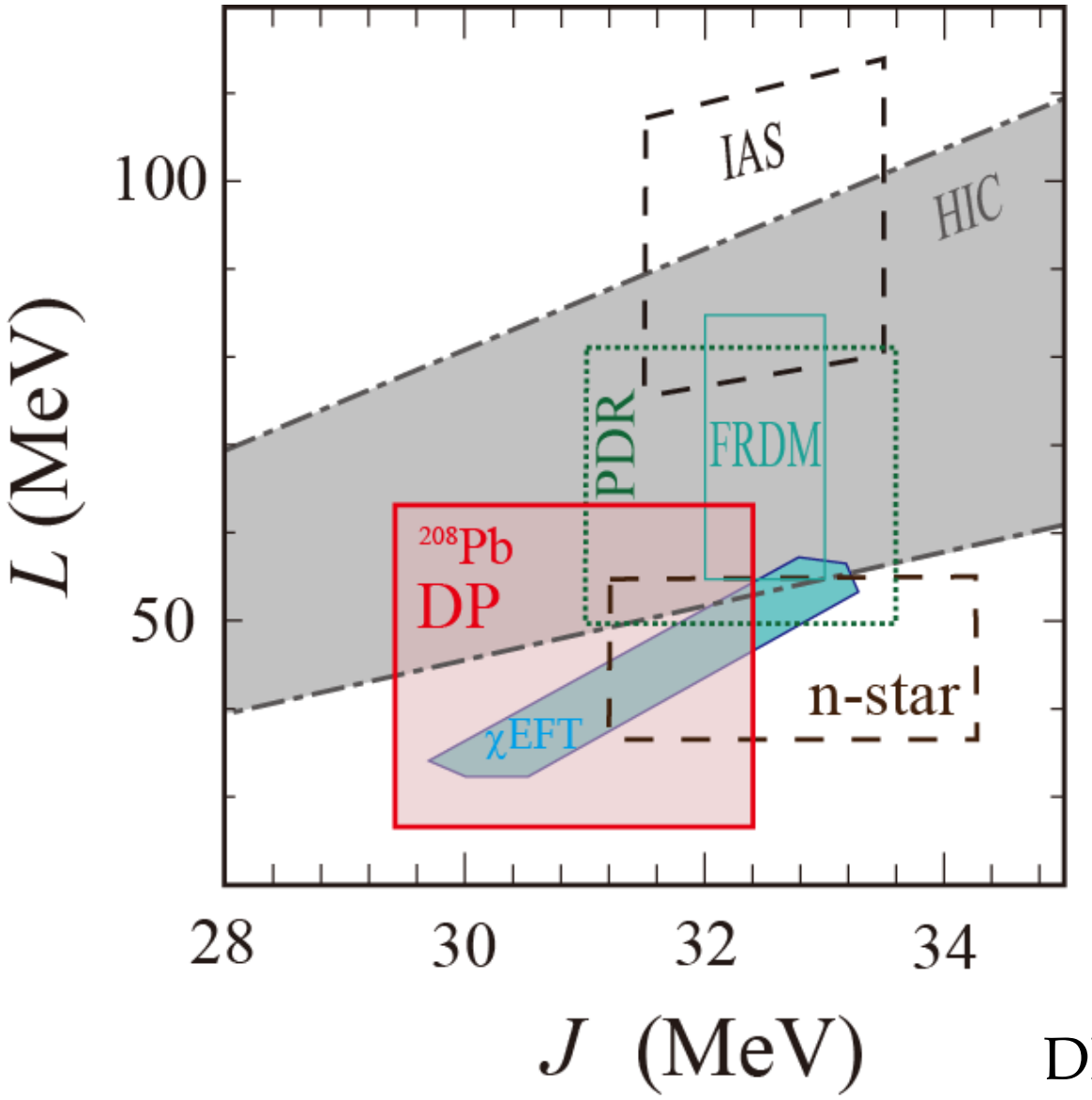

M.B. Tsang *et al.*,
PRC**86**, 015803 (2012).

I. Tews et al.,
arXiv:1206.0025v1

and this work

DP: Dipole Polarizability
HIC: Heavy Ion Collision
PDR: Pygmy Dipole Resonance
IAS: Isobaric Analogue State
FRDM: Finite Range Droplet Model (nuclear mass analysis)
n-star: Neutron Star Observation
χEFT: Chiral Effective Field Theory

Preliminary

DP: L=45±18 MeV
J=30.9±1.5 MeV

Theoretical Correction by C.J. Horowitz

C.J. Horowitz et al., PRC85,032501(R)(2012)

Firstly Woods-Saxon shape weak density distribution is assumed

$$\rho_W(r) = \frac{\rho_0}{1 + \exp[(r - R)/a]}, \qquad (2)$$

With fixing a=0.6 fm, R is changed so as to the acceptance average of A

$$\langle A \rangle = \frac{\int d\theta \sin\theta \, \epsilon(\theta) \frac{d\sigma}{d\Omega} A_{pv}}{\int d\theta \sin\theta \, \epsilon(\theta) \frac{d\sigma}{d\Omega}}. \qquad (4)$$

reproduced the PREX result

$$A_{\rm pv}^{\rm Pb} = 0.656 \pm 0.060 \ (\text{stat}) \pm 0.014 \ (\text{syst}) \ \text{ppm}. \qquad (5)$$

Then the R=6.982 fm is obtained. With this $\rho_w(r)$, and the equation

$$F_W(q) = \frac{1}{Q_W} \int d^3r \frac{\sin qr}{qr} \rho_W(r). \qquad (3)$$

$F_w(q\text{-bar})$ has been determined as (q-bar = 0.475±0.003 fm^{-1})

$$F_W(\bar{q}) = 0.204 \pm 0.028 \ (\text{exp}) \pm 0.001 \ (\text{mod}). \qquad (6)$$

Why can the model dependence be obtained with only change a and fixing ?

The model uncertainty (0.001) has been obtained by varying a by ±0.05 fm.

The range of a was obtained from several mean field calculations.

Are the number of model calculations enough to estimate the model dependence?

TABLE I. Least squares fits of Wood Saxon (R, a, see Eq. (2)) or Helm model (R_0, σ, see Eq. (8)) parameters to theoretical mean field model weak charge densities.

	Wood Saxon		Helm	
Mean field force	R (fm)	a (fm)	R_0 (fm)	σ (fm)
Skyrme I [8]	6.655	0.564	6.792	0.943
Skyrme III [9]	6.820	0.613	6.976	1.024
Skyrme SLY4 [10]	6.700	0.668	6.888	1.115
FSUGold [11]	6.800	0.618	6.961	1.028
NL3 [12]	6.896	0.623	7.057	1.039
NL3p06 [6]	6.730	0.606	6.886	1.010
NL3m05 [6]	7.082	0.605	7.231	1.012
Average		0.61 ± 0.05		1.02± 0.09

Helm-model is used to extract the weak-charge radius (R_w).

Helm-model: Gaussian (with σ) is folded with a square uniform distribution with a radius R_0. The parameter σ represents the surface diffuseness and neutron size.

$$R_W^2 = \frac{3}{5}\left(R_0^2 + 5\sigma^2\right). \qquad (9)$$

Is this toy-model (Helm-model) enough for the discussion?

R_w has been determined so that the Helm-model reproduce the $F_w(q\text{-bar})$ result (equation 6). The model dependence has been estimated by varying σ with σ=1.02 ±0.09 fm. Again this σ range was estimated from mean-field calculations.

$$R_W = 5.826 \pm 0.181\ (\text{exp}) \pm 0.027\ (\text{mod})\ \text{fm}. \qquad (10)$$

Why are the two models, Woods-Saxon shape and Helm-model, used?

The weak-charge skin has been obtained as

$$R_W - R_{\rm ch} = 0.323 \pm 0.181\ (\rm exp) \pm 0.027\ (\rm mod)\ \rm fm. \quad (11)$$

The weak-charge density is expressed as

$$\rho_W(r) = 4 \int d^3r' \left[G_n^Z(|\mathbf{r} - \mathbf{r}'|)\rho_n(r') + G_p^Z(|\mathbf{r} - \mathbf{r}'|)\rho_p(r') \right]. \quad (14)$$

The single proton/neutron weak-charges are described as

$$4G_p^Z = q_p G_E^p + q_n G_E^n - G_E^s, \quad (15)$$

$$4G_n^Z = q_n G_E^p + q_p G_E^n - G_E^s. \quad (16)$$

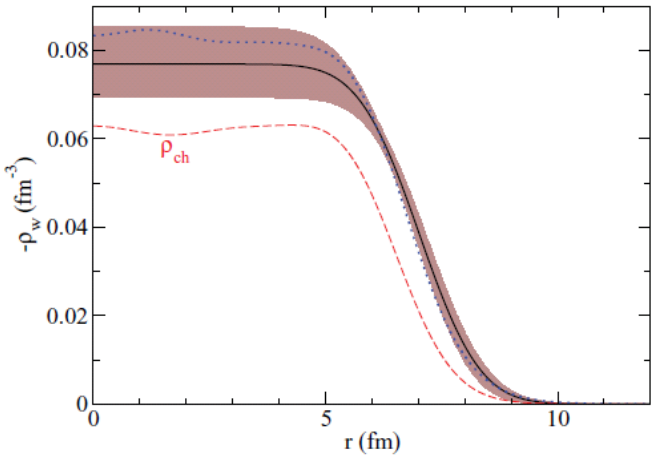

FIG. 1. (Color online) Helm model weak charge density $-\rho_W(r)$ of ^{208}Pb that is consistent with the PREX result (solid black line). The brown (gray) error band shows the incoherent sum of experimental and model errors. The red dashed curve is the experimental (electromagnetic) charge density $\rho_{\rm ch}$ and the blue dotted curve shows a sample mean-field result based on the FSUGold interaction [11].

At tree level, the weak nucleon charges are

$q_n = -1$

$q_p = 1 - 4\sin^2\vartheta_W$

where ϑ_W is the Weinberg angle., With radiative corrections,

$q_n = -0.9878$

$q_p = 0.0721$

Then

$$R_n = 5.751 \pm 0.175\ (\rm exp) \pm 0.026\ (\rm mod) \pm 0.005\ (\rm str)\ \rm fm. \quad (21)$$

$$R_n - R_p = 0.302 \pm 0.175\ (\rm exp) \pm 0.026\ (\rm mod) \pm 0.005\ (\rm str)\ \rm fm. \quad (22)$$

This model uncertainty is already larger than the model-dependence of the dipole-polarizability.

DP: R_n-R_p = 0.168 ± 0.022 fm

PREX-II Approved by PAC (Aug 2011)

"A" Rating 35 days to run in 2013 or 2014

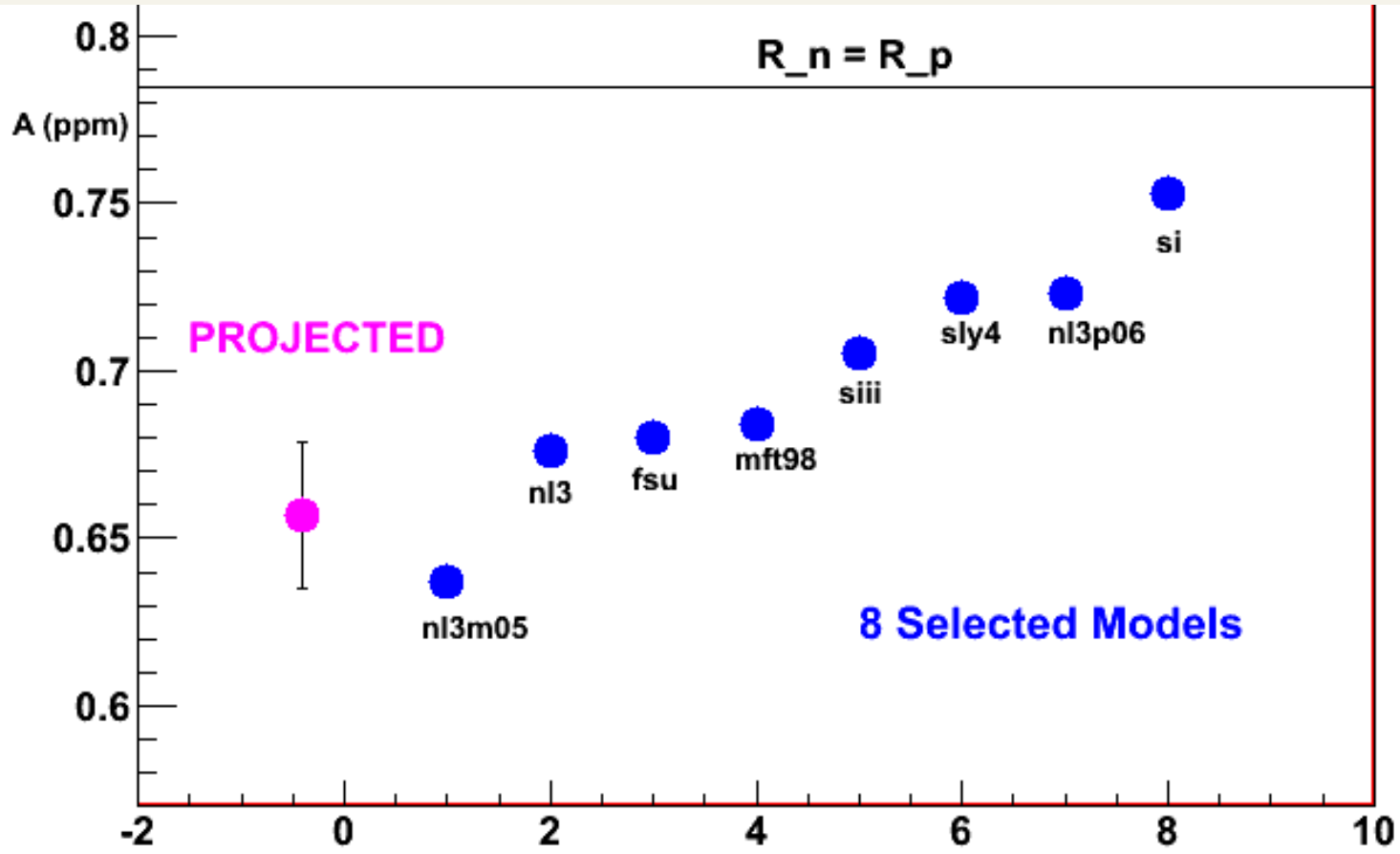

Recent R_n Predictions Can Be Tested By PREX at Full Precision

PREX could provide an electroweak complement to R_n predictions from a wide range of physical situations and model dependencies

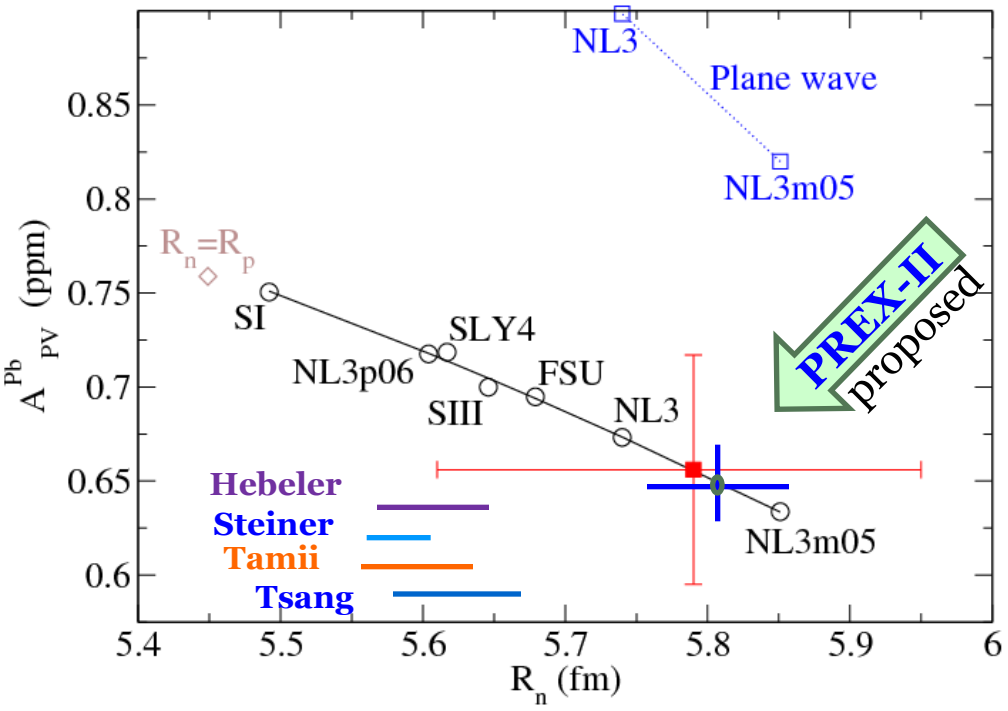

These can be tested with

$$\delta(A_{PV})/A_{PV} \sim 3\%$$

$$\delta(R_n)/R_n \sim 1\%$$

Recent R_n predictions:

Hebeler *et al*. Chiral EFT calculation of neutron matter. Correlation of pressure with neutron skin by Brown. Three-neutron forces!

Steiner *et al*. X-Ray n-star mass and radii observation + Brown correlation. (Ozel *et al* finds softer EOS, would suggest smaller R_n).

Tamii *et al*. Measurement of electric dipole polarizability of ^{208}Pb + model correlation with neutron skin.

Tsang *et al*. Isospin diffusion in heavy ion collisions, with Brown correlation and quantum molecular dynamics transport model.

Improvements for PREX-II

Region downstream of target

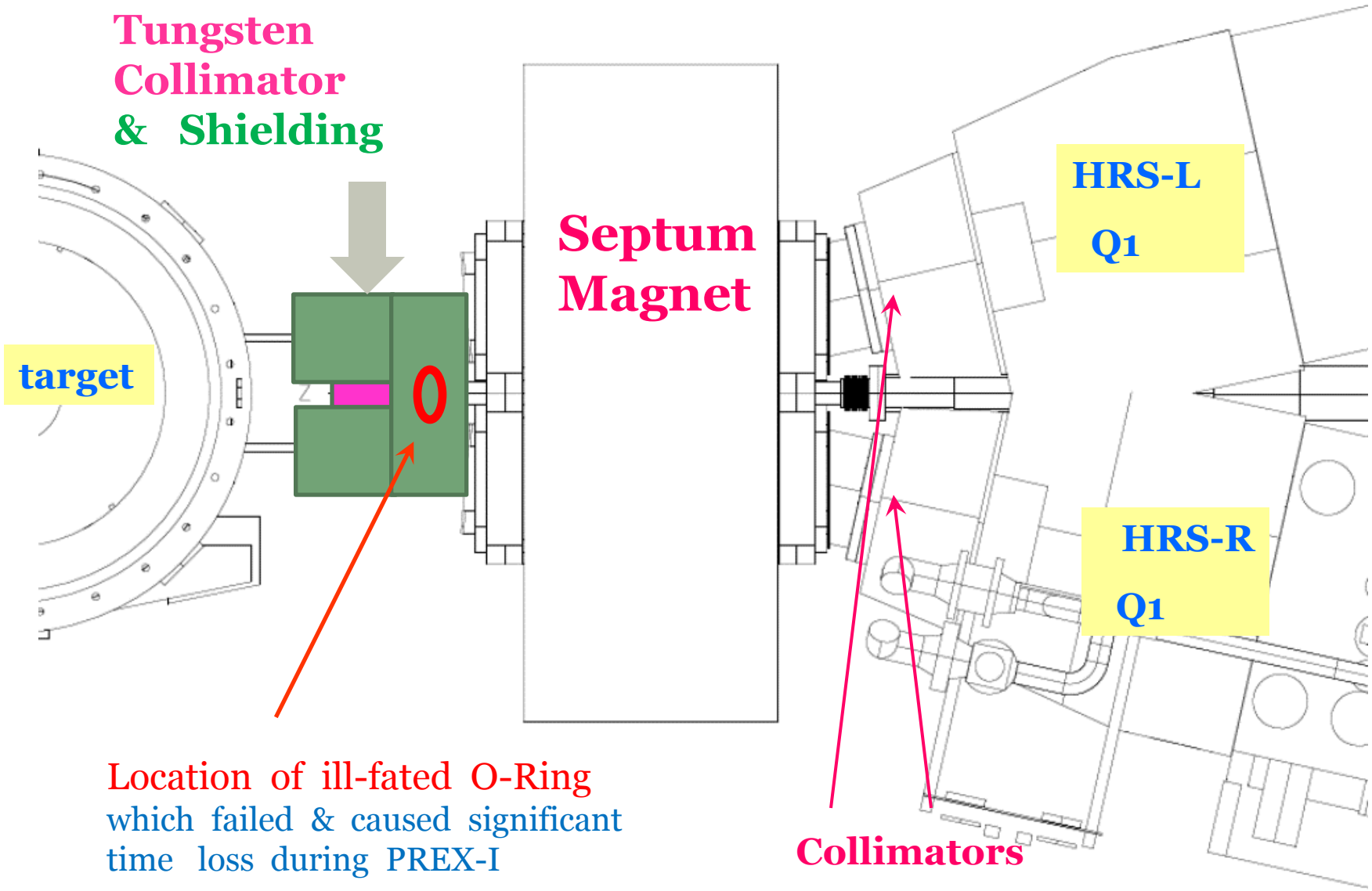

Location of ill-fated O-Ring
which failed & caused significant
time loss during PREX-I

→ **PREX-II to use all-metal seals**

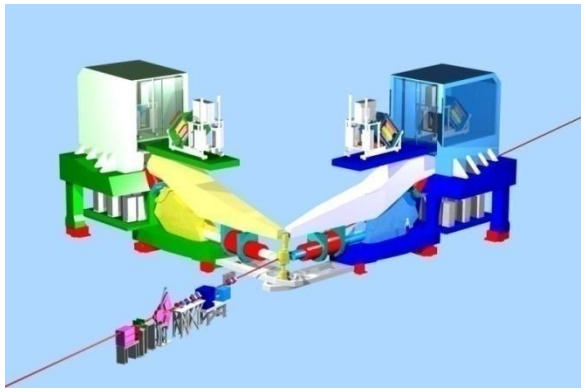

Possible Future PREX Program ?

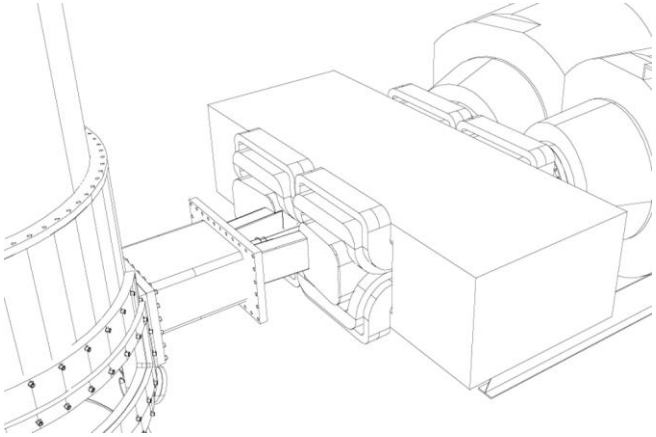

Each point 30 days stat. error only

Nucleus	E (GeV)	dR_N / R_N	comment
^{208}Pb	1	1 %	**PREX-II** (approved by Jlab PAC, A rating)
^{48}Ca	2.2 (1-pass)	0.4 %	natural 12 GeV exp't will propose @ next PAC
^{48}Ca	2.6	2 %	surface thickness
^{40}Ca	2.2 (1-pass)	0.6 %	basic check of theory
tin isotope	1.8	0.6 %	apply to heavy ion
tin isotope	2.6	1.6 %	surface thickness

Not proposed

Shufang Ban, C.J. Horowitz, R. Michaels J. Phys. G39 014104 2012

Thank you for your attention!